Sustainable Chemistry and Pharmacy 39 (2024) 101505

Contents lists available at ScienceDirect

Sustainable Chemistry and Pharmacy

journal homepage: www.elsevier.com/locate/scp

Hydrothermal conversion of Cu-laden biomass to one-step doped hydrochar used as a potential adsorbent for 2-nitrophenol removal

Dalia Allouss, Antoine Dupont, Inès Esma Achouri *, Nicolas Abatzoglou

Group of Research on Technologies and Processes (GRTP), Department of Chemical and Biotechnological Engineering, Université de Sherbrooke, Sherbrooke, QC J1K 2R1, Canada

ARTICLE INFO

Keywords:
Hydrothermal carbonization
Contaminated biomass
Hydrochar
2-Nitrophenol removal
Adsorption
Waste management

ABSTRACT

Moving towards a circular economy offers a viable path to mitigating stress on natural resources. This study revealed that hydrothermal carbonization can effectively valorize Cu-loaded spent biomass into a Cu-enriched hydrochar to be used as sorbent of organic pollutants. The structural properties and surface analysis of the obtained hydrochars were assessed using various techniques, and its adsorption capacity was evaluated through the removal of 2-nitrophenol from artificially contaminated aqueous solutions in batch adsorption tests. Central Composite Design and the Response Surface Methodology were utilized to optimize the hydrothermal carbonization process. The study was aimed at examining the individual and combined effects of hydrothermal temperature and residence time on hydrochars yield and their specific surface area. The N_2 adsorption/desorption showed that Cu-SG biomass-derived hydrochar exhibited a higher specific surface area compared with raw biomass-derived hydrochar. The results obtained indicate that the hydrochar produced at 210 °C with a 5 h reaction time (HC-210-5) is a highly efficient adsorbent for 2-nitrophenol, exhibiting a capacity ranging from 1.3 mg/g to 7.7 mg/g at low concentrations (ranging from 5 to 50 ppm). The kinetic study reveals that the adsorption process onto HC-210-5 follows pseudo-second-order kinetics, while the equilibrium isotherms were determined using the Freundlich isotherm model. These findings endorse the viability of a one-step synthesis of Cu-doped hydrochars from Cu-contaminated biomass as a promising and efficient adsorbent for the removal of micropollutants from wastewater.

1. Introduction

Heavy metal contamination of soil and water poses a serious problem due to its resistance to degradation and toxic nature (Golia, 2023). Recently, the biosorption or phytoremediation processes for removing metal ions using biomasses has been widely investigated (Ahmad et al., 2020; Coelho Menezes et al., 2021; Orozco et al., 2023; Wang et al., 2020; Wei et al., 2021). Accordingly, the proper disposal of biomass residues containing heavy metals is imperative due to the potential release of these metals into the environment, leading to the risk of secondary pollution (Akbari et al., 2023a). Hence, several methods such as incineration, gasification, hydrothermal carbonization, and pyrolysis have gained recognition as an effective treatment for the disposal of heavy metal-contaminated biomass wastes, yielding valuable products (Cui et al., 2022; Dastyar et al., 2019; Han et al., 2018; He et al., 2019).

In recent years, research has focused on hydrothermal carbonization treatment (HTC) as an energy-efficient and chemical-free method (Akkari et al., 2023b; Xu et al., 2020). HTC is a progressively favored thermal method for converting wet biomass contaminated with heavy metals into metal-rich hydrochar (Petrović et al., 2023; Zhang et al., 2022a). It should be noted that HTC can

* Corresponding author.
E-mail address: ines.esma.achouri@usherbrooke.ca (I.E. Achouri).

https://doi.org/10.1016/j.scp.2024.101505
Received 30 November 2023; Received in revised form 15 February 2024; Accepted 17 February 2024
Available online 12 March 2024

process waste biomass at lower temperatures (180–260 °C), thus minimizing energy consumption and eliminating the need for high pressure conditions (Zhang et al., 2022a). It involves residence time from minutes to several hours and typically occurs with limited or no oxygen presence. Meanwhile, the metal species present in the biomass can proficiently customize the structure of the hydrochar (Ding et al., 2020). Studies have been carried out to convert biomass contaminated with heavy metals using hydrothermal processes. Essentially, the aim is to separate and recover heavy metals effectively, while generating a clean liquid phase for biofuels and high-value chemicals (Chen et al., 2018, 2019; Yang, 2010). For instance, Chen et al. showed that hydrothermal liquefaction of Cd-polluted rice straw and Cu-polluted Elsholtzia splendens led to a concentration of up to 95% of Cu and nearly all Cd in the hydrochar, resulting in a clean liquid phase (Chen et al., 2018). However, to date, many studies on hydrothermal conversion methods for heavy metal-contaminated biomass tend to overlook the valorization and reutilization potential of the resulting metal-rich hydrochar for diverse applications.

Considering the abundance of oxygen-containing functional groups on the surface, strong chemical reactivity, presence of metal ions, cost-effectiveness, and ease of preparation, functionalized hydrochar derived from heavy metal-rich biomass is promising as a multipurpose adsorbent for the removal of organic/inorganic pollutants from water (Zhang et al., 2022a; Zhou et al., 2022). Micropollutants, like phenols, nitrophenols and nitrobenzenes, are frequently identified in the aquatic environment, encompassing wastewater, surface water, groundwater, and drinking water, at minimal concentrations ranging from ng/L to μg/L (Luo et al., 2014; Vakili et al., 2019). In particular, the 2-nitrophenol (2-NP) raises heightened concerns because of its increased toxicity compared to other isomeric nitrophenol forms, as well as its notable stability and water solubility (Kupeta et al., 2018). Hence, it becomes imperative to develop new, cost-effective, and efficient adsorbents. Hydrochars derived from biomass, include sawdust (Chandrasekar et al., 2024), palm kernel shells (Kimbi Yaah et al., 2021), leaves of Saccarum ravannae (Sachan and Das, 2024), avocado (Pauletto et al., 2021) have been employed and investigated as adsorbents for the adsorption of micropollutants.

To date, there is a limited literature dedicated to the reutilization of hydrochar derived from heavy metal-enriched biomass for the removal of micropollutants from aqueous solutions. However, the predominant focus of existing studies revolves around the application of metal-rich bio/hydrochars, specifically obtained through the pyrolysis process, as effective adsorbents for a range of pollutants including methylene blue (Gong et al., 2018), ciprofloxacin (Ding et al., 2020), phosphate (Mosa et al., 2018; Zeng et al., 2013), tetracycline (Zhou et al., 2022), and heavy metals (Jiang et al., 2023; Liu et al., 2021; L. Zhou et al., 2022). For instance, a newly developed magnetic hydrochar, derived from iron rich Phytolacca acinosa Roxb., serves as a cost-effective and efficient adsorbent for the removal of Cd from water (Liu et al., 2021). They demonstrated that the elimination of Cd by magnetic nano-Fe_3O_4 hydrochar encompasses various mechanisms, including surface precipitation, surface complexation, electrostatic attraction, and ion exchange.

This study explores the feasibility of a one-step process to produce a novel Cu-supported hydrochar from copper-laden switchgrass. The hydrochar is investigated for its potential application as an adsorbent in wastewater treatment, specifically targeting organic micropollutants. Laboratory batch sorption tests were conducted, focusing on the removal of 2-NP at low concentrations. The study aims to: (1) propose an efficient technique for converting heavy metal-contaminated biomass into metal-rich hydrochar; (2) investigate the impact of hydrothermal treatment conditions on the physicochemical characteristics of Cu-rich hydrochar to identify optimal conditions for high specific surface area; and (3) assess the optimized hydrochar's potential as an effective adsorbent for 2-NP removal from aqueous solutions.

2. Experimental

2.1. Materials

The switchgrass biomass (SG) residues used in this study were obtained from the research institute of plant biology, Montreal botanical garden (Guidi Nissim and Labrecque, 2023). The SG was washed with tap water, and rinsed with distilled water, then oven-dried at 105 °C for 12 h. The cleaned and dried samples were ground, sieved (500 μm), and placed in bags for subsequent use. In electronic supporting information (ESI), Table S1 lists the physicochemical characteristics of switchgrass biomass. All the chemicals and reagents employed in this study were of analytical quality and purchased from Sigma Aldrich. Copper nitrate trihydrate ($Cu(NO_3)_2.3H_2O$) was dissolved in de-ionized (DI) water at a concentration of 1000 mg/L to make a Cu (II) stock solution. The various concentrations of the biosorption test solution were prepared by dilution of the stock solution and the residual concentration was analyzed by atomic absorption (PerkinElmer AAnalyst 200).

2.2. Biosorption-precipitation experiments

Experimental design proves to be a useful and efficient approach in adsorption process when compared to the traditional method of changing one variable at a time (Allouss et al., 2019a; Khalifa et al., 2019; Makhado et al., 2022). Here, biosorption studies were carried out by combining independent variables (i.e., pH, temperature, time, biomass dosage, and initial concentration) using statistical methods. The Plackett-Burman design (PBD) was used to screen the factors influencing the copper biosorption-precipitation process. Furthermore, the Box-Behnken surface response methodology (BBD-RSM) was applied to optimize the process. The screening design (PBD) experiments were conducted in 250 mL conical flasks by transferring 100 mL of the necessary concentration of copper solution, with biomass dosage ranging from 2 to 4 g/L, in a batch process. Magnetic stirring of 600 rpm was applied, and the temperature was controlled using a water bath. The pH was adjusted by adding the appropriate amount of 0.1 M NaOH or 0.1 M HCl solution. The bulk solution was then filtered under vacuum using Whatman grade 1 filter paper. Next, the BBD design was employed to study the critical factors, initial Cu concentration, time, and SG dosage, identified through screening design, aiming to determine optimal conditions for maximizing the fixation of Cu on SG biomass. pH at 5 and T at 30 °C were kept constants for all BBD experimental design runs. The experimental range employed in both the screening design and BBD-RSM optimization is detailed in Table 1. A total of

Table 1
Experimental range and levels in the Placket-Burman and Box-Behnken design.

Factors	Placket-Burman Design	
	Low level (−1)	High level (+1)
Temperature (°C)	Ambient	30
Initial concentration (mg/L)	100	300
Time (h)	1	2
pH	3	5
SG dosage (g/L)	2	4

	Box-Behnken Design		
	Low level (−1)	Center (0)	High level (+1)
Initial concentration (ppm)	300	350	400
Time (min)	30	60	90
SG dosage (g/L)	4	6	8

sixteen tests were conducted for BBD design, including three repetitions at the central point, as outlined in Table S2. The adsorption capacity and removal efficiency were calculated using the specified formulas in the ESI (**Eq. S1** and **Eq. S2**, respectively).

2.3. HTC experiments

All HTC experiments were conducted in an electrically heated 1 L pressure autoclave reactor (Parker, Autoclave Engineers). In a typical experiment, around 7 g of copper-contaminated switchgrass (Cu-SG) were mixed with 105 g of distilled water in the reactor vessel. This specific water-to-biomass ratio of 15:1 was selected to guarantee efficient stirring of slurry (at speeds ranging from 300 to 500 rpm). Nitrogen was introduced into the sealed reactor for 10 min to eliminate any traces of air. Once loaded, the autoclave was initially heated to the desired HTC temperature at a specified residence time depending on self-generated pressures, an example is illustrated in Fig.S1 (ESI). Additionally, reference hydrochar from raw SG (biomass: water ratio 1:15) was prepared via hydrothermal carbonization at 200 °C and 220 °C for 6 and 2 h, respectively, in a stainless-steel reactor (Autoclave Engineers). During filtration, the solids were rinsed with distilled water and then ethanol (3 times). Minor quantities of gaseous products were present and subsequently vented. The resulting solid, called hydrochar (HC), was then dried at 105 °C for 24 h and weighed to calculate the yield. The derived hydrochars were labelled HC-180-2, HC-200-2, or HC-220-2, with the number representing the corresponding HTC temperature and residence time, respectively. The equations utilized in this experiment are as follows (Afolabi et al., 2020; Kang et al., 2012; Zhang et al., 2020).

$$Hydrochar\ yield\ (\%) = \frac{weight\ of\ dried\ hydrochar}{weight\ of\ dried\ initial\ SG\ biomass} \times 100 \quad \text{Eq. 1}$$

$$Carbon\ recovery\ (\%) = Hydrochar\ yield\ (\%) \times \frac{C\ in\ dried\ hydrochar\ (wt\%)}{C\ in\ dried\ initial\ SG\ biomass\ (wt\%)} \quad \text{Eq. 2}$$

$$Enrichement\ factor\ (EF) = \frac{C_{Cu}\ in\ hydrochar}{C_{Cu\ in\ SG\ biomass}} \quad \text{Eq. 3}$$

$$Cu\ recovery\ in\ hydrochar\ (\%) = \frac{content\ in\ hydrochar}{content\ in\ SG\ biomass} \times hydrochar\ yield \quad \text{Eq. 4}$$

A Central Composite Design (CCD) was utilized to model two responses: hydrochar yield and specific surface area, in relation to two factors, namely, HTC reaction temperature (T in °C) and residence time (t in h). it facilitates the investigation of interactions between key parameters and allows to identify the main factors for optimizing the responses. The study also explored the impact of these two factors on the structural and physico-chemical properties of the hydrochar produced through the HTC process, along with the enrichment of copper in the final product. The carbonization reaction temperatures were encoded as 180 °C, 200 °C, and 220 °C, while the residence times were encoded as 2, 4, and 6 h. The time needed to reach the desired reaction temperature was excluded from the required residence time. 2D-3D surface plots and ANOVA were obtained using Nemrodw software.

2.4. Characterization of hydrochars

Elemental contents of C, H, N, O and S (wt.%, dry basis) were measured using an Elemental analyzer (Flash, 2000 OEA, Thermo Fisher Scientific), with detection limits for N, S and O within the 0.10% range. The crystal structures of the derived hydrochars from Cu-SG biomass were examined using an X-ray diffraction (XRD) analyzer (X'Pert Pro MPD, Panalytical). The analysis comprises scanning over the diffraction angle (2θ) range of 10–80°. Thermal stability and tracking of gaseous species generated by hydrochar samples were measured on a TG (Setsys 24, Setaram) coupled to an MS analyzer (Thermostar, Pfieffer). For each experiment, approximately 8 mg of the sample was transferred to a crucible and purged with air for 10 min. Then, the sample was heated to 800 °C at a rate of 10 °C/min. Produced hydrochar, SG and Cu-SG biomasses were analyzed for N_2 adsorption-desorption isotherms at 77 K using

a gas adsorption instrument (Micromeritics, ASAP, 2020). Before adsorption, the samples were degassed at 200 ˚C overnight. The Fourier transform infrared (FTIR) spectra were recorded in the 500-4000 cm-1 wavenumber range using an Agilent Cary 630 instrument equipped with an attenuated total reflection (ATR) system. Finally, the samples' morphology and elemental compositions were assessed using high angle annular dark-field scanning transmission electron microscopy (HAADF-STEM, TFS Spectra Ultra), equipped with an energy X-ray detector (Ultra-X EDS). Samples were deposited on a perforated carbon film on nickel TEM grids suspended in alcohol.

2.5. 2-Nitrophenol adsorption test

Batch adsorption experiments were conducted in glass beakers, containing 50 mL of a 10 ppm 2-nitrophenol (2-NP) solution, and the appropriate quantity of HC-210-5 adsorbent was added. The experiments were carried out at a temperature of 25 ˚C. The beakers were continuously stirred at 200 rpm using a magnetic stirrer for varying time intervals over a total of 120 min. After the experiments, the remaining concentration of 2-NP was determined using UV-VIS spectrophotometer (Ultrospec 2100 pro) at a wavelength of 350 nm, corresponding to the maximum peak absorbance of 2-NP, and this was determined through the utilization of a calibration curve. The adsorption capacity of the adsorbed 2-NP on HC-210-5 hydrochar was determined using the equation mentioned in ESI (**Eq. S1**). Kinetic models are employed to assess the rate of the adsorption process and determine the step that controls the rate. In the current study, data obtained from batch experiments have been analyzed by applying pseudo-first-order, pseudo-second order, and intraparticle diffusion models. In addition, an equilibrium study of adsorption offers insights into the adsorbent's capacity. The Freundlich and Langmuir adsorption models were generated and compared.

3. Results and discussion

3.1. Copper biosorption-precipitation optimization

The Plackett-Burman Design (PBD) represents an effective way of choosing and identifying significant variables among many variables that influence the process (Cazetta et al., 2021; Li et al., 2023). The design is a two-level fractional design, using the first-order polynomial equation, and ignoring interactions between independent variables. A total of 16 PBD experiments were performed, as listed in Table S3. Out of a total of five factors, four have a significant influence on adsorption capacity: temperature, pH, initial Cu concentration and SG dosage (Fig. 1b). It was determined that pH, temperature, and initial Cu concentration positively influence the adsorption capacity (qe, mg/g), whereas SG dosage exhibits an antagonistic effect on q_e. Additionally, each factor shows its significance in the variation of removal efficiency response (Fig. 1b). Based on the Pareto plot (Fig. 1a), three factors, namely time, SG

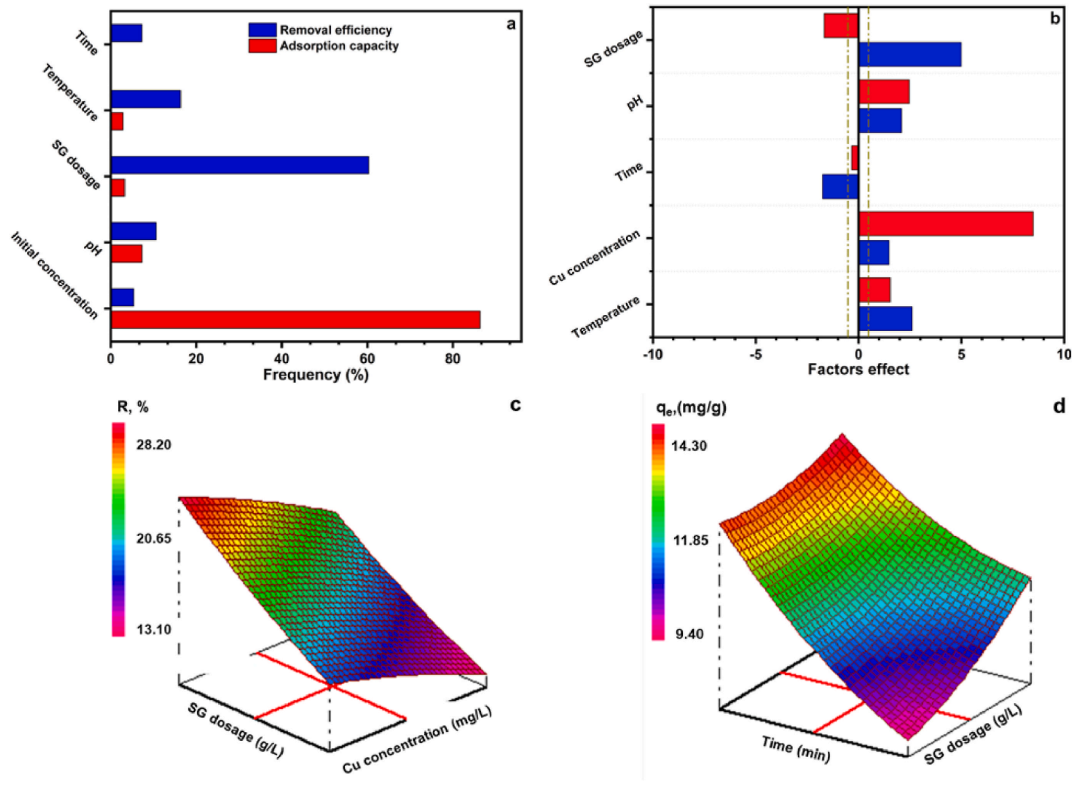

Fig. 1. (a) Pareto chart based on the PBD analysis, (b) weight of factors on the variation of two responses, 3D surfaces plots of interactive influences on (c) removal efficiency, and (d) adsorption capacity based on BBD design.

dosage and initial Cu concentration, were selected for the following optimization step via the Box-Behnken (BBD) design while keeping temperature at 30 °C and pH of 5. Table S4 presents the statistical analysis results of experimental data utilizing Fischer's test for Analysis of Variance. It furnishes comprehensive details on T-values and P-values associated with each independent variable. The model exhibited a notable agreement between the experimental R^2 value of 0.946 and the adjusted R^2 of 0.825, signifying a strong concordance. The coefficient of determination ($R^2 = 0.946$) means that 94.6% of the variability of adsorption capacity is explained by the model. According to the ANOVA analysis (Table S4), only linear terms are statistically significant. The predictive model for the adsorption capacity response can be expressed as follows (**Eq. (4)**). From **Eq. (4)**, the highest regression coefficient was achieved by SG dosage. A decrease in adsorption capacity was noted with an increase in SG dosage, as indicated by the coefficient value of −1.06, escalating from 4 g/L to 8 g/L.

$$Y = 11.85 - 1.06\ SG\ dosage + 0.67\ time\ - 0.72\ initial\ Conc + 0.45\ SG\ dosage * SG\ dosage + 0.31\ time * time - 0.68\ initial\ conc * initial\ conc + 0.47\ SG\ dosage * time + 0.66\ SG\ dosage * initial\ conc - 0.02\ time * initial\ conc \quad \text{Eq. 5}$$

3D surface plots were employed to examine the impact of individual variables and their interactions on the predicted responses related to both removal efficiency and adsorption capacity. Surface profile analysis is essential to study the mutual interactions between variables. Fig. 1c illustrates a 3D surface plot showing the combined effect of SG dosage and initial copper concentration on removal efficiency while the contact time was set to its zero level (t = 60 min). It was evident that an elevation in SG dosage could enhance the removal efficiency of Cu(II). Biomass dosage is a crucial parameter, as it defines the capacity of a biosorbent under specific operating conditions for a given initial concentration (Benkaddour et al., 2020). This is attributed to the fact that a higher adsorbent dosage results in an increased surface area, providing more available adsorption sites and, consequently, leading to an important removal of Cu(II). On the other hand, A decrease in adsorption capacity was noted with an increase in SG dosage, as indicated by the coefficient value of −1.06, escalating from 4 g/L (13.20 ± 1.40 mg/g) to 8 g/L (10.15 ± 1.38 mg/g) (Fig. 1d). According to the 3D plots, the predicted value of optimum Cu (II) removal and adsorption capacity were found to be (21.39 ± 4.43) % and (11.25 ± 1.40) mg/g, respectively, with the use 6 g/L of SG biomass, Cu(II) concentration of 300 mg/L during 30 min of agitation time. After the biosorption step, the slurry (Cu(II) solution with SG biomass) underwent precipitation by the addition of sodium hydroxide (NaOH, 0.5 M) to achieve a pH of 7, with an additional 30 min of agitation. The purpose of this precipitation step was to concentrate Cu from the solution onto the SG biomass. Cu^{2+} dominates as the primary species involved in adsorption below a pH of 6.0 (Allouss et al., 2019b). In addition, $Cu(OH)^+$ starts forming around pH 4 to 5, while $Cu(OH)_2$ precipitates at pH levels above 6, indicating incomplete removal via adsorption. The hydroxyl ions engage with the metal ions to create hydroxide precipitates, leading to a decrease in free metal ions, in addition to the hydrolysis of metallic ions. Table 2 displays the concentration of Cu in SG biomass acquired through both the biosorption process and the combined biosorption-precipitation method. Therefore, the copper content in SG biomass becomes extremely high when the combined biosorption and precipitation method is used. Therefore, pH-induced precipitation is a straightforward process that can be coupled with biosorption to mimic biomass contamination through phytoremediation process (Kafle et al., 2022).

3.2. HTC process optimization

CCD was employed to investigate the optimal levels of two factors: hydrothermal temperature and time on hydrochar yield and its specific surface area. Analysis of variance was utilized to evaluate the predicted models (Table S5). The findings suggested that the quadratic model better predicted the coefficients of the mathematical models. The P-values obtained for both models were below 0.05, confirming the significance of the presented models. In addition, the lack-of-fit values for the responses relating to HC yield and the specific surface area were 0.211 and 0.184 respectively. Also, the R^2 and $R^2_{Adjusted}$ values are 0.984, 0.957, 0.995 and 0.987 respectively, which indicates a good fit. The coefficient estimations result of HC yield and specific surface area are given in Table 3.

The terms for which the p-value is less than 5% are considered significant. In this case of HC yield response, temperature (X_1) and its quadratic term (X_1^2), plus the interaction term (X_1X_2), have a p-value of less than 5% and are therefore selected as highly significant model terms. Based on data in Table 3, both temperature and time have a negative impact on the variation of hydrochar yield, whereas these two factors positively influence the specific surface area response. A comparable trend was noted for hydrochar derived from liquorice root pulp employing both catalytic and non-catalytic hydrothermal carbonization (Akbari et al., 2023a). Fig. 2a shows that the hydrochar yield is influenced by both the hydrothermal temperature and residence time.

An increase of both factors results in a decrease in hydrochar yield, creating a curved response surface. Furthermore, the highest specific surface area is achieved at the boundaries of the CCD experimental domain Fig. 2c. Yet, the hydrothermal temperature had a greater impact on hydrochar yield compared to residence time. A similar trend was observed in the hydrothermal carbonization of used coffee grounds (Afolabi et al., 2020). The final CCD for HC yield and S_{BET} responses, which includes significant quadratic terms,

Table 2
The concentration (mg/kg) of Cu in SG biomass.

Samples	Cu concentration (mg/kg)	Cu wt.%
Cu-SG from biosorption process	7799.8	0.8
Cu-SG from biosorption-precipitation process	43 760.7	4.4

Table 3
coefficient estimation and statistics.

Response	Terms	Coefficient	t-value	p-value (%)
HC yield (%)	Constant	50.16	52.45	0.01
	Temperature: X_1	−7.55	−8.86	0.303
	Time: X_2	−2.26	−2.65	7.7
	X_1X_2	4.00	3.46	4.05
	X_1^2	−8.66	−7.70	0.455
	X_2^2	0.88	0.78	49.0
S_{BET} (m^2/g)	Constant	6.90	14.36	0.07
	Temperature: X_1	3.89	9.09	0.282
	Time: X_2	4.957	11.60	0.137
	X_1X_2	−2.925	−5.03	1.51
	X_1^2	5.260	9.30	0.263
	X_2^2	4.260	7.53	0.486

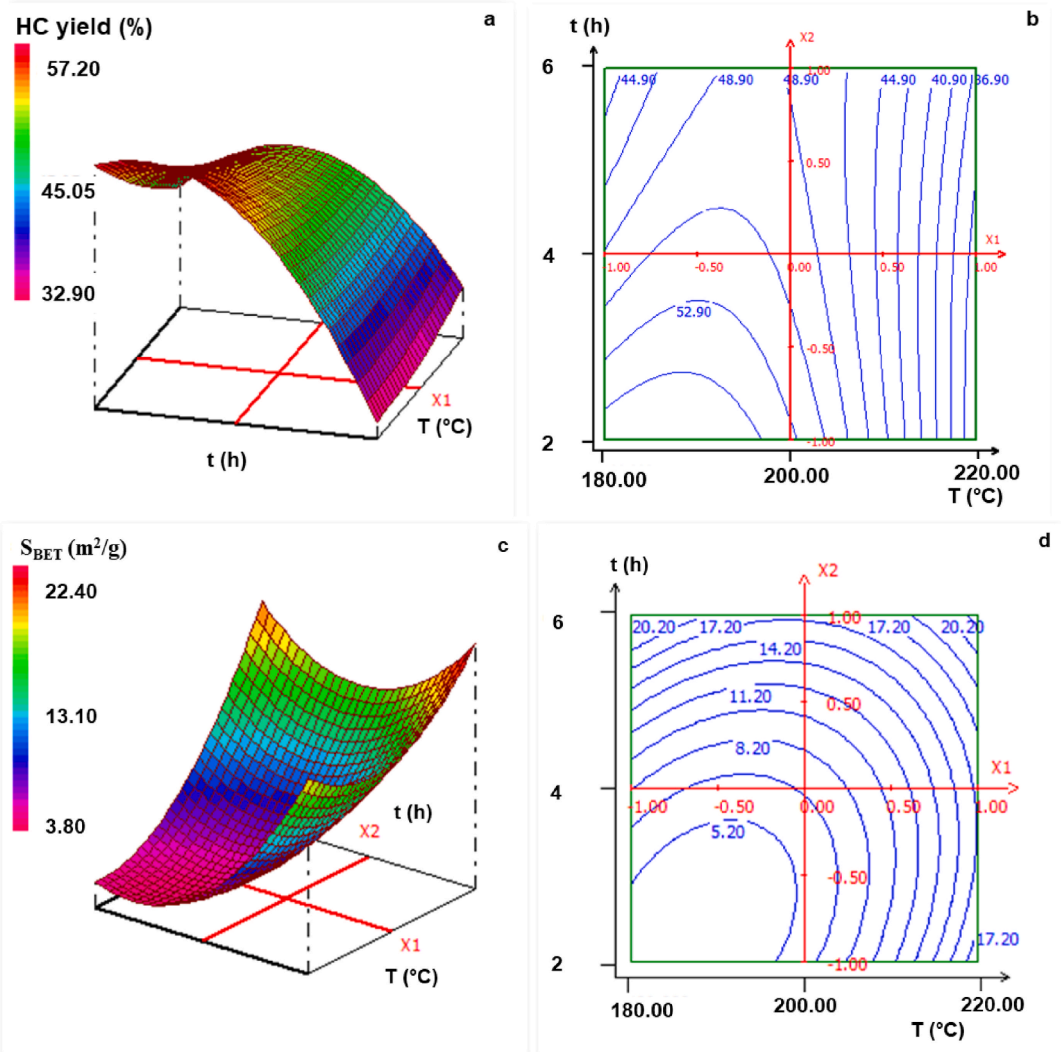

Fig. 2. (a), (c) 3D response surface plots, and (b), (d) 2D contour plots illustrating the influence of temperature (T) and time (t) under different operational conditions on HC yield and S_{BET}.

represents a mathematical quadratic polynomial model that correlates the responses with the two selected variables in the current HTC process and can be written as follows:

$$HC\ yield\ (\%) = 50.16 - 7.56\ T - 8.67\ T^{*}T + 4.01\ T * t \quad \text{Eq. 6}$$

$$S_{BET}\ \ (m^2/g) = 6.91 + 3.89\ T + 4.98\ t + 5.26\ T^{*}T + 4.26\ t * t - 4.01\ T * t \quad \text{Eq. 7}$$

The optimal operating conditions, as suggested by Nemrodw software, were determined to be 210 °C and 5 h residence time to achieve a maximum hydrochar yield along with a significant specific surface area. The predicted and experimental HC yields were 43.05% and 43.7% respectively, confirming the model's validity under optimum operating conditions. In addition, the predicted and experimental specific surface area were 12.7 m^2/g and 11.6 m^2/g, respectively. The HC-210-5 hydrochar was then used to remove 2-NP from aqueous solutions.

3.2.1. Product distribution and Cu content in hydrochar

Temperature is of paramount importance in the thermal treatment (Jain et al., 2016). Thus, we investigated the effect of temperature variation and reaction time on hydrochar yields during hydrothermal treatment of Cu-laden SG biomass at temperatures from 180 to 220 °C. Fig. 3 illustrates the quantitative outcomes of the products distribution, showcasing the conversion of Cu-SG biomass into three distinct products of interest at different temperatures and residence time: liquid organics (L), hydrochars (S), and gases (G) as well as the effect of residence time at different hydrothermal temperature on hydrochar yield in the terms of the mass of Cu-SG biomass. Residence time exerts a direct impact on hydrochar production, with a shorter residence time resulting in higher solid hydrochar yield, and conversely, a longer residence time leading to lower solid hydrochar yield (Fig. 3a). This occurred because the Cu-SG biomass underwent hydrolysis, leading to its dissolution in water or partitioning into gas and liquid phases (Fig. 3b–c, and Fig. 3d). The reaction temperature significantly influences hydrochar characteristics, exhibiting an almost-linear correlation with carbon content (Table S6). Consequently, as the temperature increases, the carbon yield decreases.

The impact of hydrothermal temperature and time on Cu recovery in hydrochar is detailed in Table 4. The concentration of Cu in hydrochar was higher than in SG biomass, as confirmed by the enrichment factor calculations. With an increase in residence time (for temperatures of 200 and 220 °C), there was a notable rise in the concentration of Cu in hydrochar, leading to a significant enhancement in Cu recovery within the hydrochars. This is attributed to the formation of metallic copper in the hydrochar (Zhang et al., 2006). Conversely, for a hydrothermal temperature of 180 °C, an opposing trend was observed.

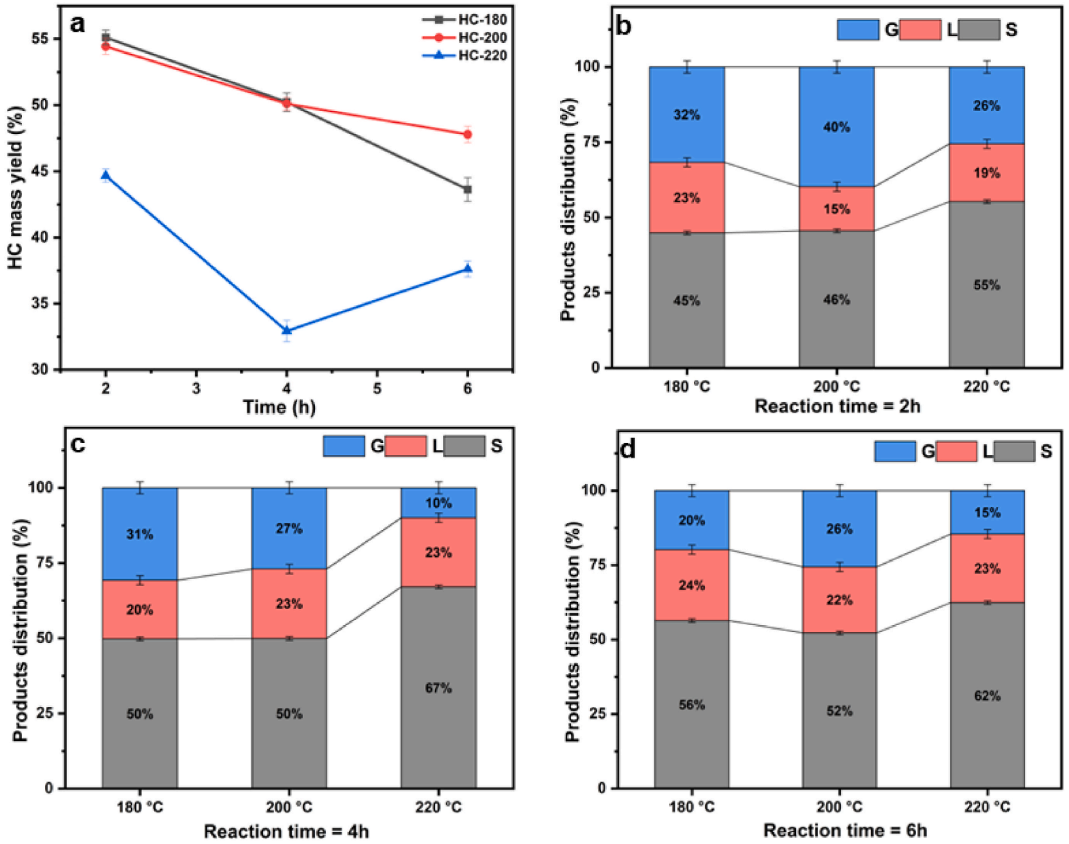

Fig. 3. (a) Effect of residence time on hydrochar mass yield at different hydrothermal temperatures, (b) Hydrothermal carbonization product distribution at different residence time (b) 2h, (c) 4h and (d) 6h.

Table 4
Content of Cu in hydrochar formed by HTC at different temperature and time conditions.

Sample	Cu recovery in char (%)	Enrichment factor
HC-180-2	95.9	1.7
HC-180-4	88.9	1.8
HC-180-6	71.0	1.6
HC-200-2	72.7	1.3
HC-200-4	74.1	1.5
HC-200-6	94.6	2.0
HC-220-2	79.7	1.8
HC-220-4	73.3	2.2
HC-220-6	86.6	2.3

3.3. Characterization of Cu-enriched hydrochar

3.3.1. Elemental analysis

Ultimate analysis of raw SG biomass, Cu-SG and derived hydrochars is performed using H/C and O/C atomic ratios and plotted using a Van Krevelen diagram (Fig. 4). The hydrothermal carbonization of Cu-SG biomass leads to an increase of the carbon content of the solid residue, transitioning from 45.1% by weight in the initial biomass to a range of 47.4%–56.6% by weight in the hydrochar samples (see Table S6). The low carbon content and elevated H/C and O/C atomic ratios in the structure of hydrochars produced in short times affirm the limited advancement of carbonization reactions, indicating the presence of volatile compounds with lower density in their structure.

A decrease in oxygen and hydrogen content is observed in the samples. These changes are consistent with the development of a more condensed material. It has been found that an elevation in hydrothermal carbonization temperature (i.e., from 180 °C to 220 °C) causes a decrease in O/C and H/C atomic ratios. This indicates that the degree of condensation of hydrochar products has increased. Same trend is observed with residence time; shorter reaction times produce less condensed hydrochars (high O/C and H/C atomic ratios).

3.3.2. Morphology and microstructure properties

The morphological behavior of copper nanoparticles recovered in hydrochar is an interesting aspect of this study. At 180 °C hydrothermal temperature, copper nanoparticles are irregular in shape, indicating a more random and uncontrolled pattern to their growth (Fig. 5). However, as hydrothermal temperature increased, a significant morphological change occurred on the copper nanoparticles. At the 220 °C hydrothermal temperature, more geometric and defined shapes appeared. STEM images indicated the Cu recovered in the hydrochars formed irregular shapes, mostly polygons, squares, and some clustered aggregated spherical particles. All indicate crystalline structures of the Cu particles.

The morphological characteristics of Cu-enriched hydrochar samples indicate that Cu particles were loaded onto the hydrochar and developed individually (Wei et al., 2020). Furthermore, microcrystalline layers were observed in the HC-220-6 sample (Fig. 6), providing evidence for the presence of graphite (Moretti et al., 2019). The graphitized carbon layers consist of approximately 50–60 layers, with an interlayer distance measuring about 0.37 nm (Fig. S4). This indicates that copper in hydrochar plays a catalytic role in forming ordered crystalline graphite layers via the mechanism of metal-catalyzed graphitization (Liu et al., 2019).

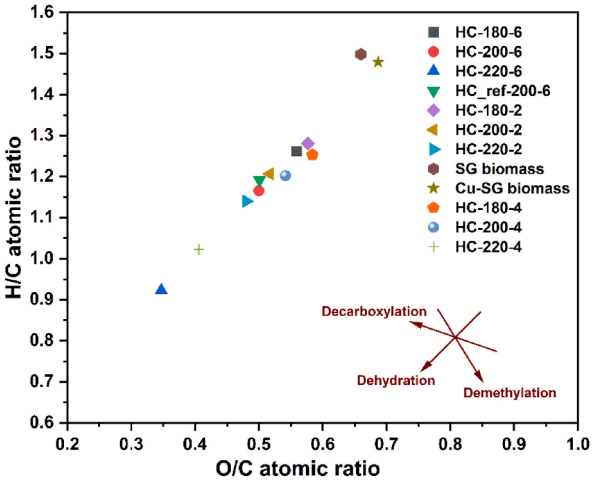

Fig. 4. Van Krevelen diagram for SG, Cu-SG biomasses and hydrochars.

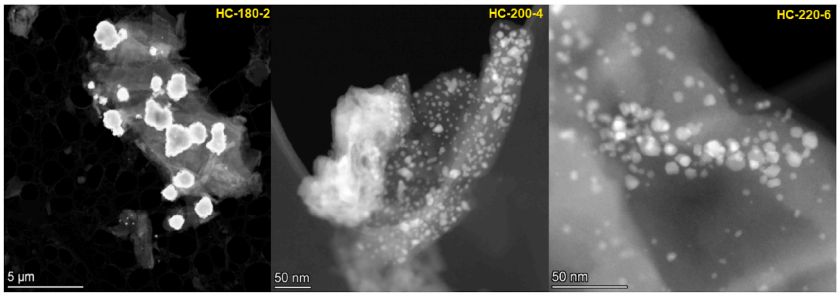

Fig. 5. TEM image of Cu-enriched hydrochar produced at different temperatures.

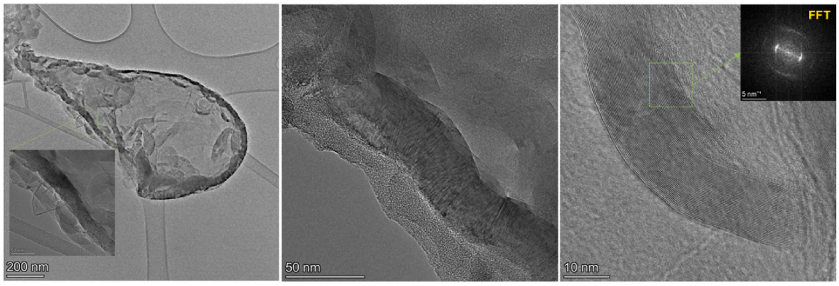

Fig. 6. HRTEM images of HC-220-6 and the corresponding FFT image of the pristine graphite.

Fig. 7 illustrates elemental mapping images of HC-210-5, revealing a predominant presence of carbon (C), oxygen (O), and copper (Cu) elements in the prepared hydrochar (Table 5). Additionally, a significant presence of sulfur is observed in the same location as copper, suggesting that the sulfur present in the solution was taken by copper-rich hydrochar.

3.3.3. Crystallographic properties

Powder X-ray diffraction (XRD) was utilized for the characterization of both chemical composition and crystallographic structure, as well as for determining the crystallite size of the samples (Lin et al., 2022). XRD patterns of hydrochar derived Cu-SG biomass and reference hydrochar samples are shown in Fig. 8. Here, the crystalline lattice structure of the cellulose was clearly apparent at 15.36° and 22.46° (Sevilla and Fuertes, 2009; Zhang et al., 2015) treatment at 180 °C. As the duration of the HTC reaction increased, the intensity of the diffraction of the cellulose crystals diminished more noticeably. In addition, when the reaction temperature was elevated from 180 to 220 °C, the crystalline structure of the cellulose disappeared (Lin et al., 2022; Sevilla and Fuertes, 2009). When comparing the hydrochar derived from raw biomass and that from Cu-contaminated biomass, clear differences in the hydrochar patterns were observed.

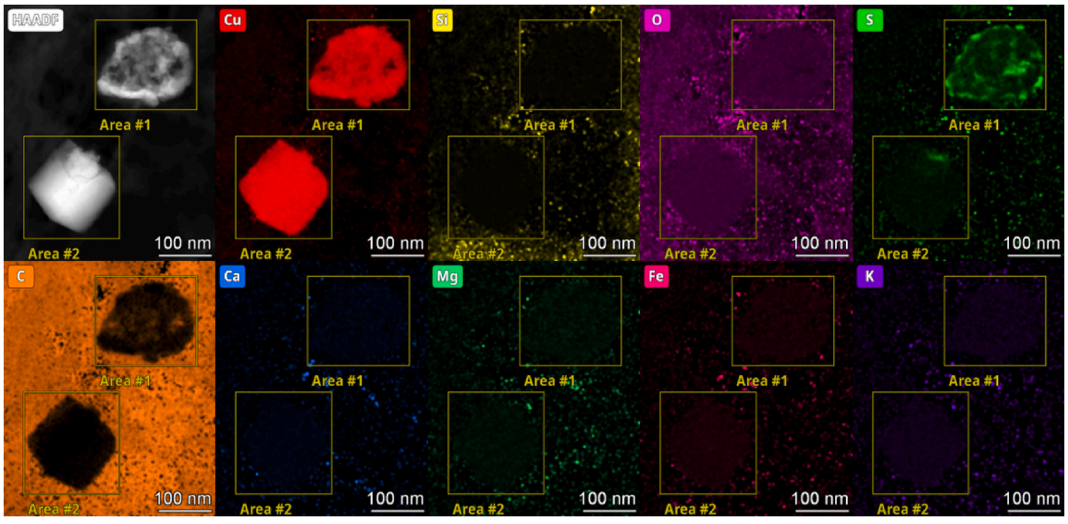

Fig. 7. HAADF-STEM image of hydrochar produced at 210 °C during 5 h of residence time and its relative elemental mapping.

Table 5
Quantitative HAADF STEM analysis.

	Element	Atomic Fraction (%)	Mass Fraction (%)
Area 1	C	48.20 ± 2.61	21.68 ± 1.98
	Cu	25.83 ± 2.93	61.45 ± 3.70
	Si	0.14 ± 0.03	0.14 ± 0.03
	O	19.17 ± 3.19	11.49 ± 2.27
	S	1.50 ± 0.29	1.80 ± 0.37
	Ca	0.01 ± 0.00	0.02 ± 0.00
	Mg	0.06 ± 0.01	0.05 ± 0.01
	Fe	0.12 ± 0.02	0.26 ± 0.04
Area 2	C	30.34 ± 2.30	11.04 ± 1.20
	Cu	37.88 ± 3.90	72.92 ± 3.37
	Si	0.13 ± 0.03	0.11 ± 0.02
	O	25.44 ± 4.05	12.33 ± 2.52
	S	0.40 ± 0.08	0.38 ± 0.08
	Ca	0.01 ± 0.00	0.01 ± 0.00
	Mg	0.09 ± 0.02	0.07 ± 0.02
	Fe	0.15 ± 0.02	0.25 ± 0.04

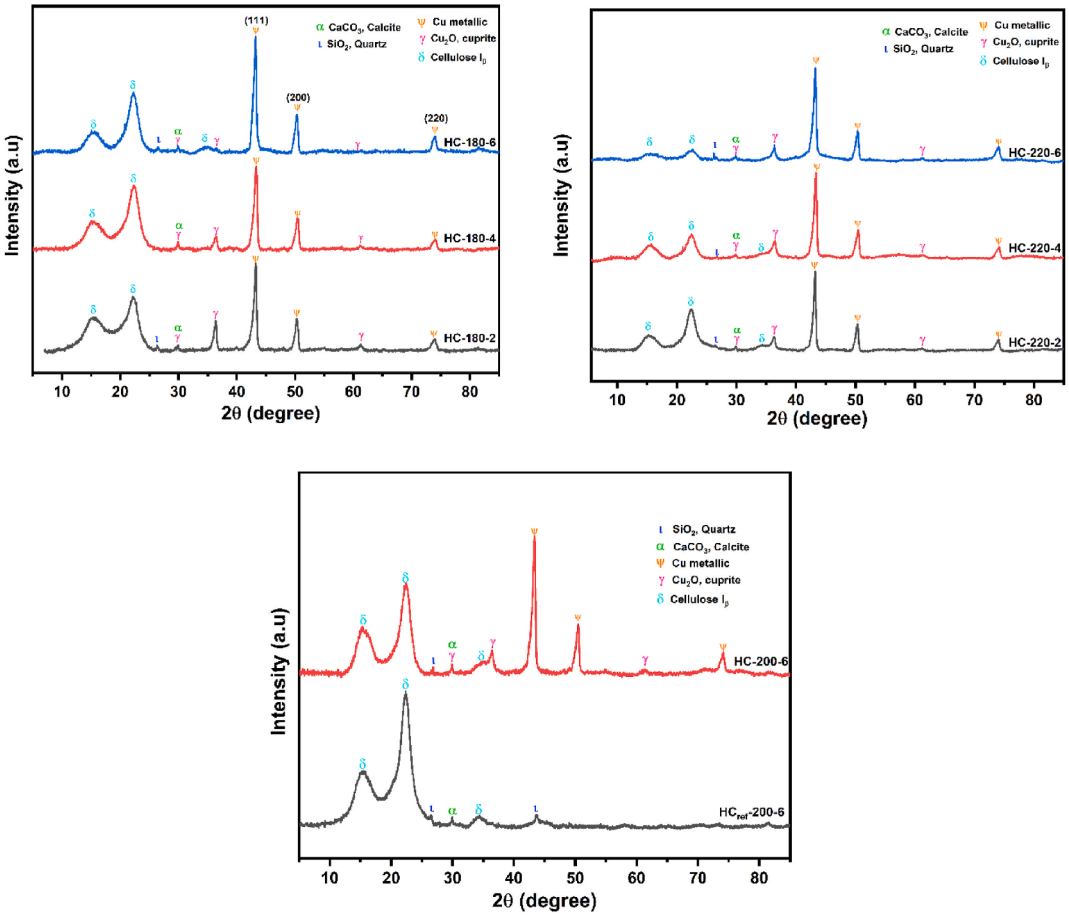

Fig. 8. XRD patterns of hydrochars derived Cu-Switchgrass biomass at different temperatures.

Most peaks in the XRD patterns in Fig. 8 are easily distinguishable, indicating a high degree of crystallinity in the Cu-SG biomass derived hydrochar samples. The XRD analysis indicated that the copper ions initially present in the SG biomass underwent chemical reduction to Cu and Cu_2O. This reduction process occurred concurrently with the consumption of hydroxide ions generated through the self-ionization of water (Eivazihollagh et al., 2017). The diffraction peaks at $2\theta = 43.24$, 50.34 and 74.02 may be indexed as the (111), (200) and (220) planes of copper exhibiting a cubic symmetry for the hydrochars produced from Cu-SG biomass. In addition, the peaks at 29.85°, 36.55° and 61.33° correspond to the (111), (200), (220) and (311) crystallographic plans of the body centered cubic Cu_2O phases, respectively (Ben Moussa et al., 2023; Liaqat et al., 2024). By applying the Scherrer equation, the crystallite size of

copper was calculated based on the broadening of diffraction peaks, indicating a slight increase by increasing the residence time. It is assumed that the line broadening of peaks due to chemical disorder and mechanical strain is negligible. It was observed that, with a varying residence time, the crystallite size of copper increased from 14.3 nm for HC-180-2 to 15.7 nm for HC-180-6. In addition, the crystallinity index of the HC-180-2 was figured to be 70% and it increased in the case of HC-180-6 to75% **(Table S7)**.

3.3.4. Surface chemical properties

FTIR spectra offer valuable insights into the surface functional groups within the produced hydrochars and potential interfacial interactions that may occur during the HTC process. Fig. 9 illustrates the ATR-FTIR spectra for SG, Cu-SG and their derived hydrochars. The spectra of the hydrochar produced at 220 °C distinctly deviate from the Cu-SG biomass spectrum, implying the existence of a chemical interaction between the biomass conversion and copper.

A broad band in the range of 3400–3300 cm−1, associated with O–H stretching, was identified in SG biomass, Cu-SG (Fig. 9a), and the resulting hydrochars (Fig. 9b). The O–H stretching observed can be attributed to moisture content or the presence of hydroxyl and phenol groups. For HC-220-6, we observed a diminished O–H group intensity, likely because of dehydration process (Kim et al., 2014). Peaks within the 2950-2800 cm^{-1} range, associated with aliphatic C–H stretching, were present in all samples. The peak at approximately 1700 cm^{-1} can be attributed to the stretching of C = O bonds, which are found in functional groups such as ketones, aldehydes, quinones, esters, and carboxylic acids. The peak at 1510 cm^{-1} was assigned to the asymmetric stretching of –C = O in carboxylic groups. In addition, the peak at 1232 cm-1 in the pristine SG biomass is attributed to O–H bending vibration of carboxylic groups. The Cu-SG biomass and the derived hydrochars both displayed a prominent and wide peak at around 1034 cm^{-1} and 1026 cm^{-1}, respectively, indicative of the C–*O*–C vibrations related to the pyranose ring. Additionally, they can also be attributed to the stretching of *-Si-*O bonds, indicating the presence of SiO_2, which aligns with the XRD results (He et al., 2013). However, the peak intensity decreased in the hydrochar as the residence time varied, indicating the degradation of cellulose and hemicellulose. The peak at 901 cm^{-1} is attributed to β-glycosidic linkages in cellulose. This peak disappears with increasing residence time, indicating the degradation of cellulose (C A et al., 2023) The peak at 617 cm−1 is attributed to the vibrational mode of Cu(I)–O in hydrochars (Eivazihollagh et al., 2017).

3.3.5. Thermal stability behavior

The thermal stability of the Cu-biomass feedstock and the resulting hydrochars was examined using TGA/DTA in combination with mass spectroscopy (MS), and the respective TG and DTA profiles are presented in Fig. 10.

There were several distinct stages in the decomposition of the Cu-SG biomass and its hydrochars. It started with a dehydration phase, as shown by the DTG profile (Fig. 10, red line), where small discrete peaks were observed at around 73 °C (Fig. 10b). The dehydration stage took place over a temperature range from 24 °C to 133 °C for the hydrochar (HC-220-6) and from 25 °C to 128 °C for the Cu-SG biomass, peaking at 76 °C (Fig. 10a). This corresponds to the evaporation of adsorbed water, capillary water and volatile light organic products present in all samples (Afolabi et al., 2020; Kumar Mishra, 2022; Tu et al., 2021). This can clearly be seen from the weight loss rate of around 3% for hydrochars and around 6% for Cu-SG biomass. This is also confirmed by the release of H_2O between 90 and 100 °C detected by MS analysis (Fig. S5). The second stage (180–510 °C) represents the maximum decomposition where hemicellulose, cellulose and some lignin products decompose into smaller components, with 84% mass loss found for HC-220-6 (Fig. 10a). During this stage, the hydrochar is subjected to two main reactions: decarbonylation (CO and H_2O generation) as well as decarboxylation (CO_2 generation). At temperatures above 500 °C, the weight loss becomes negligible, and the weight stays relatively stable above 500 °C.

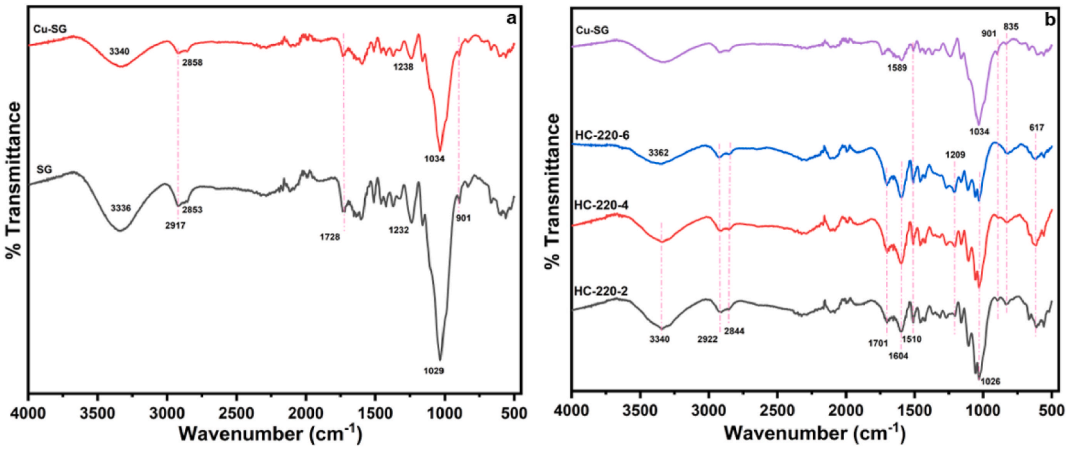

Fig. 9. ATR-FTIR spectra of a) uncontaminated and Cu-contaminated SG, and b) Cu-SG derived hydrochars.

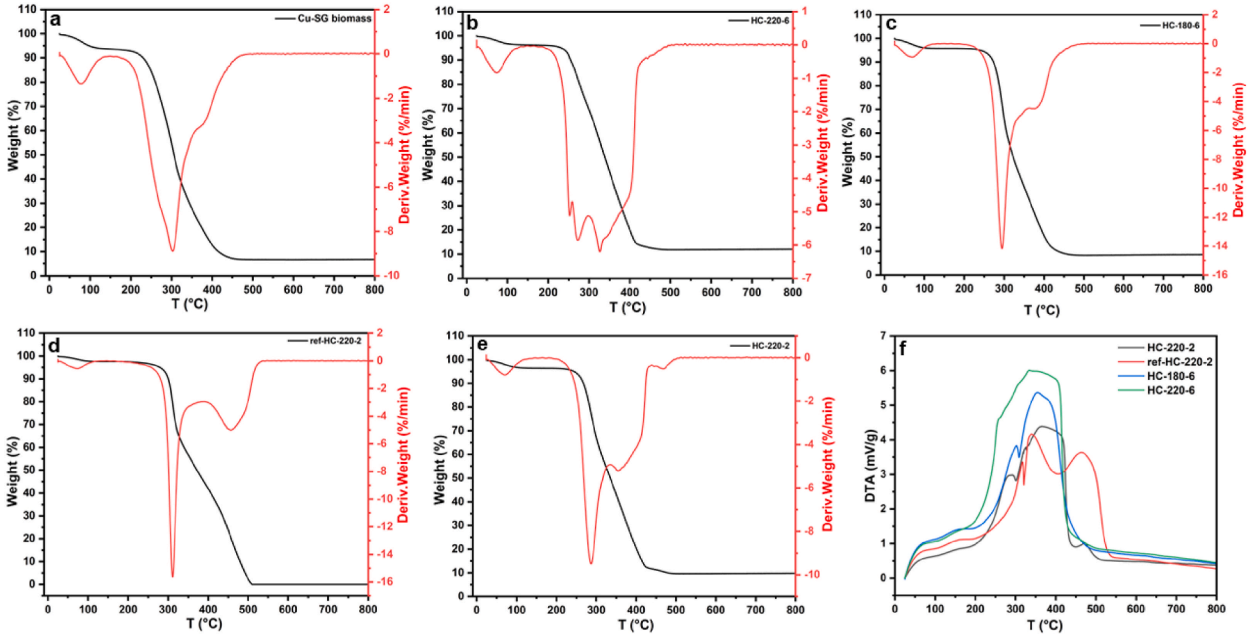

Fig. 10. TGA-DTA profiles for the produced Cu-rich hydrochars.

3.3.6. Surface area analysis

The N_2 adsorption/desorption isotherms for the hydrochars produced from Cu-SG biomass at 180 °C and 220 °C for various reaction times are illustrated in Fig. 11, with more detailed data available in Table 3. By means of the adsorption-desorption isotherm, the BET specific surface area was determined from the BET equation.

The adsorption isotherms of the derived hydrochars showed type V characteristics, indicative of mesoporous material (Alothman, 2012). An H3-type hysteresis loop is clearly apparent, for instance, between $p/p^\circ = 0.6$ and 0.99 for HC-180-2 and between 0.45 and 0.99 for HC-180-6 (Fig. 11). The H3-type hysteresis loop, without limiting adsorption to high p/p°, is usually linked to the formation of plate-shaped particles and non-rigid structure (Alothman, 2012), resulting in the formation of cleavage-sheet pores. In addition,

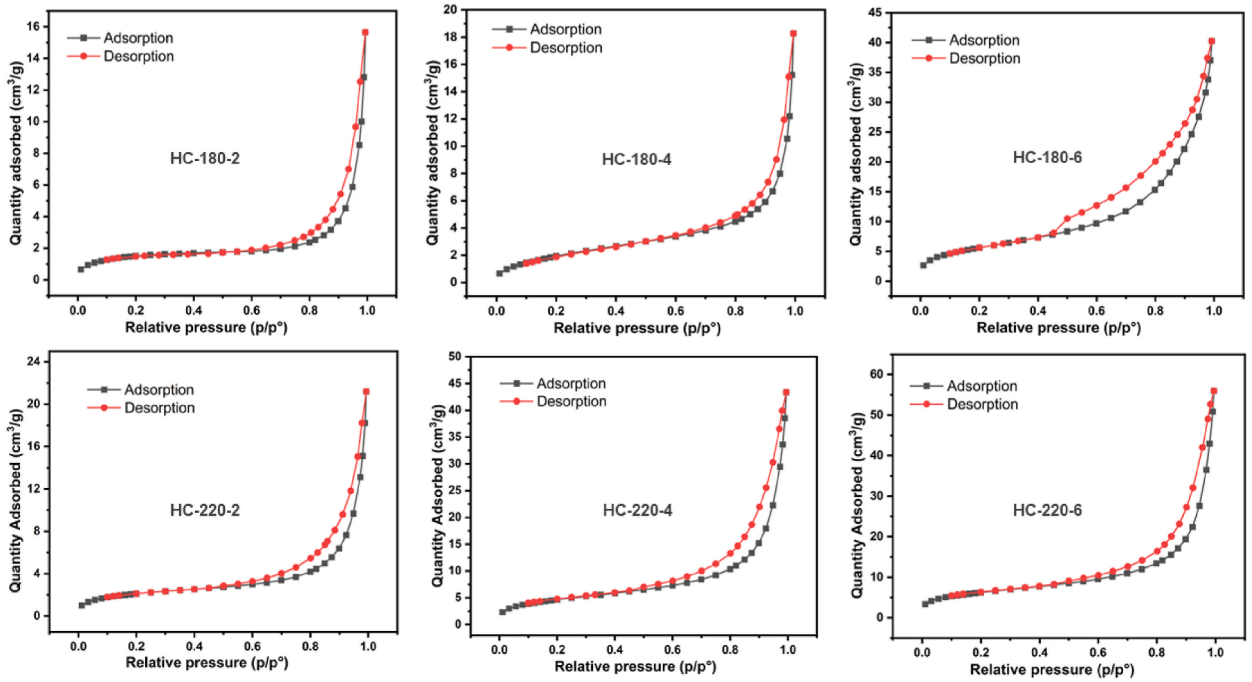

Fig. 11. Nitrogen adsorption–desorption isotherms for Cu-SG biomass derived hydrochars.

hydrochars produced at high hydrothermal temperature (220 °C) during a 6 h reaction exhibit a higher BET surface area compared to those generated at lower temperature (180 °C) within 2 h of reaction, indicated that the BET surface area increased as the residence time increased (Table 6). This could be explained by the increased formation of oxygen-containing functional groups on the surface during the hydrothermal carbonization process (Congsomjit and Areeprasert, 2021; Gao et al., 2013). Overall, high temperature and long residence times result in an increase in surface area due to increased carbonization and the development of a porous structure (Kozyatnyk et al., 2023). As the temperature rises during HTC, more carbonization reactions occur, leading to the formation of a greater number of carbon structures. This can create additional micropores and mesopores, helping to increase pore surface area and volume (X. Zhang et al., 2022b). Furthermore, the presence of Cu, both in the hydrochar and the biomass, contributes to an enhanced BET surface area (Chai et al., 2022; Raheem et al., 2022) (see Table 6).

The results of the conversion of Cu-contaminated switchgrass into hydrochar show a high BET specific surface area compared to values reported in the literature (Danso-Boateng et al., 2022; Liu et al., 2021; Sachan and Das, 2024). For instance, the magnetic nano-Fe3O4 hydrochar prepared from iron-rich Phytolacca acinosa Roxb has a BET surface area of 17.47 m^2/g at 180 °C for 8 h (Liu et al., 2021). Jiang et al. employed the HTC process to convert Sedum Alfredii Hance, a Cd/Zn hyperaccumulator, into hydrochar and KOH-activated hydrochar. Additionally, they found that the specific surface area values were only 1.74 m^2/g and 3.47 m^2/g (Jiang et al., 2023). They clarified that the channels within the hydrochars remained incompletely opened at the relatively low hydrothermal temperature, thereby accounting for the lower surface area values.

3.4. 2-Nitrophenol adsorption study

3.4.1. Adsorption kinetics

To investigate the impact of contact time on the adsorption process's efficiency, batch adsorption experiments were carried out with a constant adsorbent dose of 2 g/L and an initial 2-NP concentration of 10 ppm (initial solution pH = 4.64 ± 0.01). The contact time was systematically varied from 2 to 90 min. At specified time intervals, samples were collected from the beaker to measure the remaining 2-NP concentration in the solution. Fig. 12a illustrates the influence of contact time on the adsorption of 2-NP onto HC-210-5. It is evident that the 2-NP removal rate increased rapidly in the initial 20 min, followed by a slower uptake of 2-NP until 80 min, likely due to the saturation of adsorption sites. The rapid achievement of equilibrium within 90 min and the notable 52% removal efficiency of 2-NP by HC-210-5 emphasize the effectiveness of this adsorbent material. However, it is essential to highlight that most prior studies have focused on higher 2-NP concentrations (Arasteh et al., 2010; Kupeta et al., 2018), regarding its adsorption behavior at lower concentrations.

Pseudo-1st-order, pseudo-2nd-order and intraparticle diffusion models have been applied individually in fitting the experimental data to explain the adsorption kinetics of 2-NP on the HC-210-5 adsorbent. The linear and non-linear equations of these kinetic models were presented in the **ESI**. The linear plots of the three kinetic models as well as the calculated parameters are shown Fig. 12 and Table 7, respectively**.** Typically, the choice of the best fit can be guided by the correlation coefficient (R^2) and the predicted q_e value. For the pseudo-1st-order kinetic model, a regression coefficient (R^2) of around 0.94 was obtained. However, the calculated q_e value exhibited a considerable deviation from the experimental value, suggesting that the experimental data does not fit well within the pseudo first order model. The R^2 value for the pseudo-2nd-order kinetic model at a concentration of 10 ppm is higher than that of the pseudo-1st-order model. Additionally, the calculated q_e value ($q_{e,calc}$ = 2.64 ± 0.01 mg/g) shows a more reasonable match with the experimental value ($q_{e,exp}$ = 2.61 ± 0.02 mg/g). Hence, it can be concluded that the adsorption of 2-NP conforms to the pseudo-2nd-order kinetic model, indicating that the adsorption efficiency of 2-NP mainly depends on the number of available active sites of the HC-210-5 adsorbent (Kupeta et al., 2018). This kinetic model suggests that the rate-limiting step could involve a chemisorption process characterized by valence forces (Liu et al., 2016). Similar findings were also reported by Arasteh et al. when studying the kinetics of 2-NP adsorption onto multi-wall carbon nanotubes (Arasteh et al., 2010). Given the complex nature of the adsorption process, it is plausible that a combination of pseudo-second order and pseudo-first-order kinetic models are involved, suggesting both chemical and physical adsorption interactions between adsorbent and adsorbate.

Furthermore, the involvement of intraparticle diffusion kinetic model was investigated by plotting q_t against $t^{1/2}$ (Fig. 12d). the relationship between q_t and $t^{1/2}$ exhibited linearity during three consecutive adsorption stages. It indicates that the adsorption of 2-NP

Table 6
Textural parameters of hydrochars derived Cu-contaminated switchgrass.

Samples	S_{BET} (m^2/g)	$S_{Langmuir}$ (m^2/g)	V_{total} (cm^3/g)	d_p (nm)
SG biomass	1.6	2.5	0.006	47.0
Cu-SG biomass	2.8	4.6	0.008	19.8
HC-180-2	5.2	8.1	0,02	33.3
HC-180-4	7.8	13.3	0.03	16.3
HC-180-6	20.4	32.6	0.06	11.8
HC-200-2	5.6	9.1	0.02	24.5
HC-200-4	7.0	11.0	0.02	21.3
HC-200-6	16.4	26.0	0.06	19.3
HC-220-2	7.4	11.6	0.03	23.7
HC_ref-220-2	6.4	10.3	0.03	25.6
HC-220-4	16.6	26.3	0.06	18.6
HC-220-6	21.8	34.2	0.08	18.3

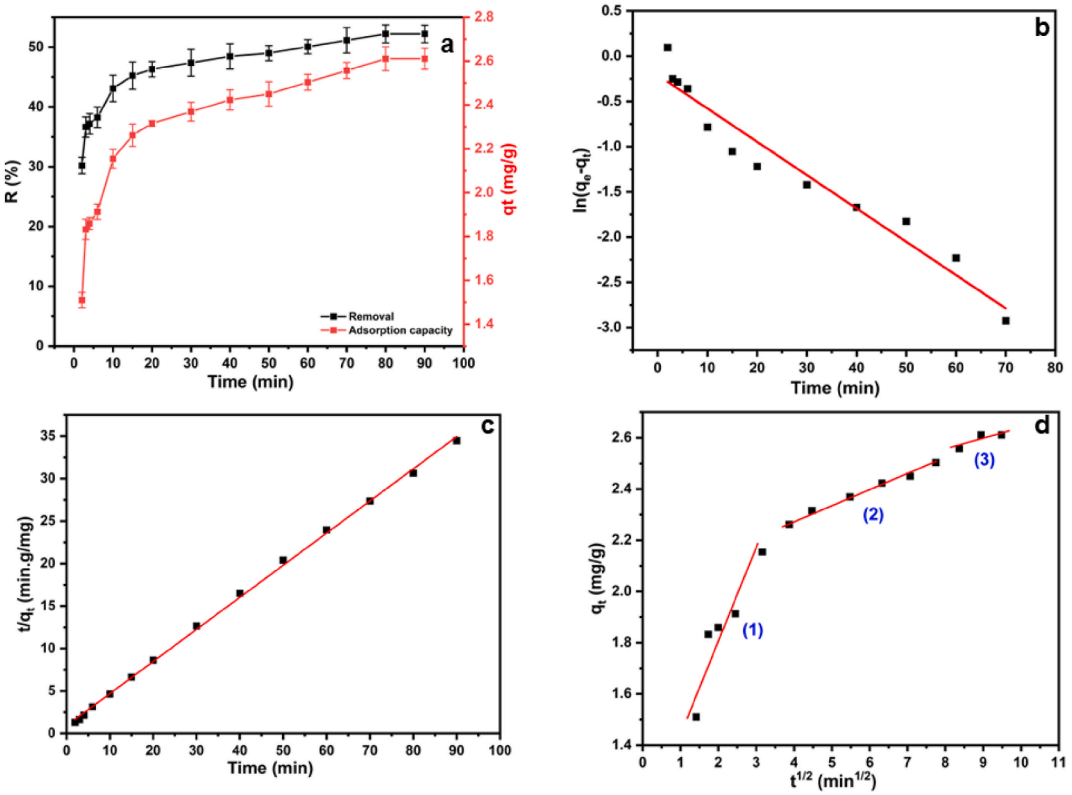

Fig. 12. (a) Contact time effect on 2-nitrophenol removal (%) and adsorption capacity (mg/g), (b) pseudo-first order, (c) pseudo-second order and (d) intra-particle diffusion kinetic models.

Table 7
Kinetic model parameters for 2-NP adsorption on the HC-210-5 material.

Kinetic models	Parameters		
Pseudo-1st-order	$q_{e,exp}$ (mg/g)		2.61 ± 0.02
	k_1 (1/min)		0.04 ± 0.09
	R^2		0.94
	$q_{e,cal}$ (mg/g)		0.8 ± 0.0
	RMSE		0.05
Pseudo-2nd-order	$q_{e,exp}$ (mg/g)		2.61 ± 0.02
	k_2 (g/mg.min)		0.2 ± 0.1
	R^2		0.99
	$q_{e,cal}$ (mg/g)		2.64 ± 0.01
	RMSE		0.15
Intraparticle diffusion	Step (1)	k_1 (mg/g.min$^{1/2}$)	0.31 ± 0.07
		C_1 (mg/g)	1.18 ± 0.17
		$r_{pearson}$	0.93
	Step (2)	k_2 (mg/g.min$^{1/2}$)	0.06 ± 0.00
		C_2 (mg/g)	2.04 ± 0.02
		$r_{pearson}$	0.99
	Step (3)	k_3 (mg/g.min$^{1/2}$)	0.05 ± 0.03
		C_3 (mg/g)	2.16 ± 0.24
		$r_{pearson}$	0.88

micropollutant by the HC-210-5 adsorbent transpired in three well-defined stages, each represented by a distinct linear plot (as shown in Fig. 12d). The rate constant k_i for each of these stages was directly determined from the slope of regression line, as listed in Table 7. The first stage corresponds to the diffusion of 2-NP molecules from the bulk solution to the external surface of the HC-210-5 adsorbent. The subsequent stage represents intra-particle diffusion, where the 2-NP molecules diffuse along the adsorbent's pores to reach the internal surface of the hydrochar. The third stage was ascribed to the attachment of 2-NP onto internal surfaces and the saturation of adsorption sites upon reaching adsorption equilibrium phase. The linearity observed in the plots presented in Fig. 12d, along with the significant R^2 values, underscores the considerable role played by intraparticle diffusion in the adsorption of 2-NP by the HC-210-5. This strongly suggests that the rate-limiting step is the intraparticle diffusion process (Ma et al., 2019).

3.4.2. Adsorption isotherms

To investigate the influence of the initial 2-NP concentration on adsorption efficiency and to gain a deeper insight into the adsorption behavior, adsorption experiments were conducted by varying the initial 2-NP concentration from 5 to 50 ppm. In this experiment, the adsorbent dosage and contact time were held constant at 2 g/L (i.e., 100 mg of HC-210-5 in 50 mL of 2-NP solution) and 90 min, respectively. The impact of 2-NP concentration on the removal efficiency (%) and adsorption capacity (mg/g) under the specified operating conditions is illustrated in Fig. 13a. Various models, including Langmuir and Freundlich isotherms (Akkari et al., 2023c), were utilized to fit the experimental data and provide an accurate description of the interaction between 2-NP and the HC-210-5 adsorbent at equilibrium. The linear and non-linear equation forms of these isotherm models are given in the **ESI**.

Fig. 13a depicts that the adsorption capacity rises from 1.3 to 7.7 mg/g as the initial 2-NP concentration increases from 5 to 50 ppm. However, the removal efficiency of 2-NP considerably decreases with the increasing initial micropollutant concentration. A higher 2-NP concentration amplifies the driving force for mass transfer from the bulk solution to the adsorbent surface, facilitating a more rapid sorbent uptake and greater adsorption capacity (Allen et al., 2005; Arasteh et al., 2010). Conversely, as 2-NP concentration increases, adsorption sites become increasingly occupied, leading to a decline in removal efficiency. Through a visual analysis of the plots in Fig. 13b and c, and considering the high R^2 (Table 8), a reasonable conclusion can be drawn that the Freundlich model provides a better description of the isotherm data for HC-210-5 adsorbent. This confirms that the adsorption of 2-NP onto the hydrochar adsorbent entails a multi-layer adsorption process on a heterogeneous surface.

3.5. Adsorbents comparison and proposed mechanism

Numerous adsorbents have been explored for the removal of 2-NP from aqueous solutions (Allen et al., 2005; Arasteh et al., 2010; Kupeta et al., 2018; Li et al., 2019; Pauletto et al., 2021) (see Table 8). In Table 9, HC-210-5 adsorbent, demonstrated competitive adsorption ability and affinity for 2-NP compared to other reported materials. Notably, this study highlights the superior performance of the Cu-rich hydrochar, particularly at lower 2-NP concentrations. Furthermore, the developed adsorbent is novel, cost-effective, and represents a sustainable approach, derived from heavy metal-contaminated biomass resulting from biosorption and phytoremediation processes (Akbari et al., 2023a; Islam et al., 2022). These features enhance the scalability and viability of the proposed disposal solu-

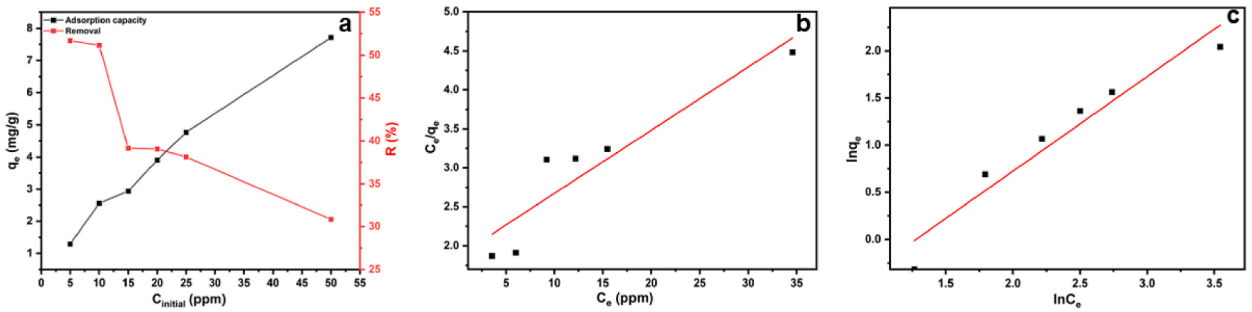

Fig. 13. (a) influence of initial 2-NP concentration on the R (%) and q_e (mg/g); linear regression plots of (b) Langmuir and (c) Freundlich.

Table 8
Isotherm parameters for 2-NP adsorption on the HC-210-5.

Isotherm models	Parameters	
Langmuir	q_{max} (mg/g)	12.57 ± 0.02
	k_L (L/mg)	0.042
	R_L	0.3 to 0.8
	R^2	0.86
	RMSE	0.132
Freundlich	k_F	0.78
	n	1.54
	R^2	0.97
	RMSE	0.011

Table 9
Adsorption capacities of various materials for 2-nitrophenol removal.

Adsorbents	C_0 (mg/L)	T (°C)	q_{max} (mg/g)	Refs
Activated carbon from water hyacinth	160	28	47.62	Isichei and Okieimen (2014)
Hydrochar from Cu-SG biomass	50	25	12.57	This study
Polyurethane cross-linked pinecone biomass	100	25	41.17	Kupeta et al. (2018)
Bentonite treated with HDMTA	100	25	18.64	Navarro et al. (2009)
Multi-wall carbon nanotubes MWNTs	310	25	476.19	Arasteh et al. (2010)
MWNTs-COOH	310	25	256.41	

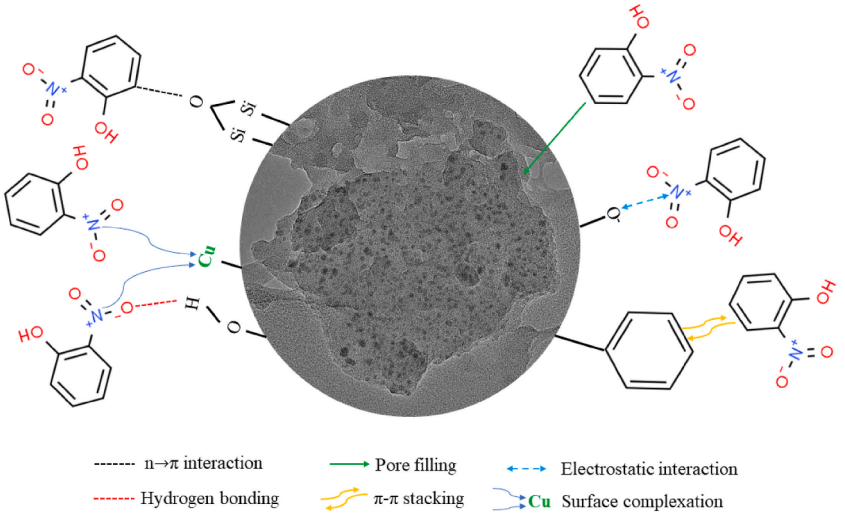

Scheme 1. Possible mechanism of 2-NP adsorption onto HC-210-5 hydrochar adsorbent.

tion, both economically and ecologically, while also opening new avenues for enhancing the efficacy of the produced hydrochar, specifically in effectively removing low concentrations of 2-NP from wastewater.

The adsorption mechanism of a contaminant onto an adsorbent relies on several factors, including the properties of the adsorbent, the nature of the adsorbate, and potential interactions between the adsorbate and adsorbent (Li et al., 2019). Aromatic compounds and carbonyl functional groups on the hydrochar surface from Cu-SG biomass, as confirmed by FTIR analysis, may contribute to the adsorption of 2-NP. The nitro group (NO_2) demonstrates pronounced electronegativity, causing a displacement of π-electrons from the aromatic ring (Allen et al., 2005; Arasteh et al., 2010), facilitating interaction with the π-electrons on HC-210-5 hydrochar. A proposed scheme illustrates the 2-NP adsorption mechanism (Scheme 1). Considering the abundance of copper in the hydrochar, it is advantageous for the nitro group to interact with Cu through surface complexation (İnci and Aydın, 2017), as reported for the nitroaromatic compounds on graphene materials (Chen and Chen, 2015).

4. Conclusion

The study highlighted a new hydrochar, derived from copper-rich switchgrass through hydrothermal carbonization, as a cost-effective adsorbent for the removal of 2-NP from synthetic aqueous media. The optimization of the HTC process, utilizing response surface methodology, revealed that the optimal operating conditions are 210 °C for 5 h, and a water-to-biomass ratio of 15:1. Within the temperature range of 180–220 °C and a duration of 2–6 h, approximately 71%–95% of copper is concentrated in the solid phase. The prepared hydrochars are mesoporous materials, with a specific surface area ranging from 5.2 to 21.8 m^2/g. In addition, STEM analysis revealed that the changes in Cu morphology within the hydrochars were observed as the hydrothermal temperature increased. Consequently, the performance of the hydrochar was assessed in a batch adsorption process for 2-NP. The maximum Langmuir adsorption for 2-NP on HC-210-5 was 12.57 mg/g. Furthermore, the adsorption process of HC-210-5 hydrochar for 2-NP was more effectively elucidated by the pseudo-2nd-order kinetic and Freundlich isotherm models. These findings indicate that the adsorption process involves a combination of physisorption (electrostatic interaction, hydrogen bonding) and chemisorption (surface complexation). The approach presented in this work facilitates the transformation of heavy-metal-contaminated biomass derived from bioremediation processes into metal-rich hydrochar. This material holds promise as an effective adsorbent for various adsorption applications.

CRediT authorship contribution statement

Dalia Allouss: Writing – original draft, Validation, Methodology, Formal analysis, Data curation. **Antoine Dupont:** Methodology, Formal analysis. **Ines Esma Achouri:** Writing – review & editing, Supervision, Investigation, Funding acquisition, Conceptualization. **Nicolas Abatzoglou:** Writing – review & editing, Supervision, Funding acquisition.

Declaration of competing interest

The authors declare that they have no known competing financial interests or personal relationships that could have appeared to influence the work reported in this paper.

Data availability

Data will be made available on request.

Aknowledgment

This research has been produced within the financial support of the 2020 Horizon Global Platform of the New Frontiers in Research Fund (NFRF) of the Government of Canada (NFFRG-2020-00117) and the Fond de recherche Société et culture (FRSC) of the Government of Québec (2022-FNFR-310130) for funding related with this work in addition to the support provided by FRQNT strategic cluster Centre SÈVE.

Appendix A. Supplementary data

Supplementary data to this article can be found online at https://doi.org/10.1016/j.scp.2024.101505.

References

Afolabi, O.O.D., Sohail, M., Cheng, Y.L., 2020. Optimisation and characterisation of hydrochar production from spent coffee grounds by hydrothermal carbonisation. Renew. Energy 147, 1380–1391. https://doi.org/10.1016/J.RENENE.2019.09.098.

Ahmad, Shamshad, Pandey, A., Vandan Pathak, V., Veer Tyagi, V., Kothari, R., Ahmad, S., Pandey Bioenergy, A., Pathak, V.V., Tyagi, V.V., Kothari, I.R., 2020. Phycoremediation: algae as eco-friendly tools for the removal of heavy metals from wastewaters. Bioremediation of Industrial Waste for Environmental Safety 53–76. https://doi.org/10.1007/978-981-13-3426-9_3.

Akbari, A., Peighambardoust, S.J., Lotfi, M., 2023a. Hydrochar derived from Liquorice root pulp utilizing catalytic/non-catalytic hydrothermal carbonization: RSM optimization and cationic dye adsorption assessment. J. Water Proc. Eng. 55, 104099. https://doi.org/10.1016/J.JWPE.2023.104099.

Akkari, I., Graba, Z., Pazos, M., Bezzi, N., Atmani, F., Manseri, A., Kaci, M.M., 2023b. Recycling waste by manufacturing biomaterial for environmental engineering: application to dye removal. Biocatal. Agric. Biotechnol. 50, 102709. https://doi.org/10.1016/J.BCAB.2023.102709.

Akkari, I., Graba, Z., Pazos, M., Bezzi, N., Manseri, A., Derkaoui, K., Kaci, M.M., 2023c. NaOH-Activated pomegranate peel hydrochar: preparation, characterization and improved acebutolol adsorption. Water Air Soil Pollut. 234, 1–17. https://doi.org/10.1007/S11270-023-06723-9/METRICS.

Allen, S.J., Koumanova, B., Kircheva, Z., Nenkova, S., 2005. Adsorption of 2-nitrophenol by technical hydrolysis lignin: kinetics, mass transfer, and equilibrium studies. Ind. Eng. Chem. Res. 44, 2281–2287. https://doi.org/10.1021/IE049455D/ASSET/IMAGES/LARGE/IE049455DF00012.JPEG.

Allouss, D., Essamlali, Y., Amadine, O., Chakir, A., Zahouily, M., 2019a. Response surface methodology for optimization of methylene blue adsorption onto carboxymethyl cellulose-based hydrogel beads: adsorption kinetics, isotherm, thermodynamics and reusability studies. RSC Adv. 9, 37858–37869. https://doi.org/10.1039/c9ra06450h.

Allouss, D., Essamlali, Y., Chakir, A., Khadhar, S., Zahouily, M., 2019b. Effective removal of Cu (II) from aqueous solution over graphene oxide encapsulated carboxymethylcellulose-alginate hydrogel microspheres : towards real wastewater treatment plants. Environ. Sci. Pollut. Control Ser. 27, 7476–7492.

Alothman, Z.A., 2012. A review: fundamental aspects of silicate mesoporous materials. 2012. Materials 5, 2874–2902. https://doi.org/10.3390/MA5122874. Pages 2874-2902 5.

Arasteh, R., Masoumi, M., Rashidi, A.M., Moradi, L., Samimi, V., Mostafavi, S.T., 2010. Adsorption of 2-nitrophenol by multi-wall carbon nanotubes from aqueous solutions. Appl. Surf. Sci. 256, 4447–4455. https://doi.org/10.1016/J.APSUSC.2010.01.057.

Ben Moussa, F., Ait-Ramdane-Terbouche, C., Terbouche, A., Belkhalfa, H., Guerniche, D., Zouaoui, A., 2023. Novel thermal synthesis of ternary Cu-CuO-Cu2O nanospheres supported on reduced graphene oxide for the sensitive non-enzymatic electrochemical detection of pyruvic acid as a cancer biomarker. J. Organomet. Chem. 989, 122638. https://doi.org/10.1016/J.JORGANCHEM.2023.122638.

Benkaddour, S., Ouahabi, I. El, Hiyane, H., Essoufy, M., Driouich, A., Antri, S. El, Hajjaji, S. El, Slimani, R., Lazar, S., 2020. Removal of Basic Yellow 28 by biosorption onto watermelon seeds, Part I: the principal factors influencing by Plackett-Burman screening design. Surface. Interfac. 21, 100732. https://doi.org/10.1016/J.SURFIN.2020.100732.

C A, A., P, N., K, K., G, V.S., 2023. Bio-based cellulose supported copper oxide nanoparticles for the reduction of nitro-aromatic compounds. Inorg. Chim. Acta. 545, 121243. https://doi.org/10.1016/J.ICA.2022.121243.

Cazetta, A.L., Spessato, L., Almeida, V.C., 2021. The use of chemometric tools for screening and optimization of variables in the preparation and application of carbon-based materials. J. Taiwan Inst. Chem. Eng. 121, 321–336. https://doi.org/10.1016/j.jtice.2021.04.004.

Chai, Y., Chen, A., Bai, M., Peng, L., Shao, J., Yuan, J., Shang, C., Zhang, J., Huang, H., Peng, C., 2022. Valorization of heavy metal contaminated biomass: recycling and expanding to functional materials. J. Clean. Prod. 366, 132771. https://doi.org/10.1016/j.jclepro.2022.132771.

Chandrasekar, R., Deen, M.A., Narayanasamy, S., 2024. Performance analysis of hydrochar derived from catalytic hydrothermal carbonization in the multicomponent emerging contaminant systems: selectivity and modeling studies. Bioresour. Technol. 393, 130018. https://doi.org/10.1016/J.BIORTECH.2023.130018.

Chen, H., Wang, X., Lu, Xilei, Xu, L., Wang, J., Lu, Xiuyang, 2018. Hydrothermal conversion of Cd-enriched rice straw and Cu-enriched Elsholtzia splendens with the aims of harmless treatment and resource reuse. Ind. Eng. Chem. Res. 57, 15683–15689. https://doi.org/10.1021/ACS.IECR.8B04378/ASSET/IMAGES/LARGE/IE-2018-04378P_0005.JPEG.

Chen, H., Wang, X., Lyu, X., Xu, L., Wang, J., Lu, X., 2019. Hydrothermal conversion of the hyperaccumulator Sedum alfredii Hance for efficiently recovering heavy metals and bio-oil. J. Environ. Chem. Eng. 7, 103321. https://doi.org/10.1016/J.JECE.2019.103321.

Chen, X., Chen, B., 2015. Macroscopic and spectroscopic investigations of the adsorption of nitroaromatic compounds on graphene oxide, reduced graphene oxide, and graphene nanosheets. Environ. Sci. Technol. 49, 6181–6189. https://doi.org/10.1021/ES5054946/SUPPL_FILE/ES5054946_SI_001.PDF.

Coelho Menezes, J.M., Maria da Silva Bento, A., José de Paula Filho, F., Martins da Costa, J.G., Melo Coutinho, H.D., Pereira Teixeira, R.N., 2021. Kinetic and thermodynamic study of copper (II) IONS biosorption by Caryocar Coriaceum Wittm bark. Sustain Chem Pharm 19, 100364. https://doi.org/10.1016/J.SCP.2020.100364.

Congsomjit, D., Areeprasert, C., 2021. Hydrochar-derived activated carbon from sugar cane bagasse employing hydrothermal carbonization and steam activation for syrup decolorization. Biomass Convers Biorefin 11, 2569–2584. https://doi.org/10.1007/S13399-020-00635-Y/METRICS.

Cui, X., Li, X., Zhang, J., Lin, Q., Xiao, H., Cheng, Z., Yan, B., Yang, X., Chen, G., 2022. Hydrothermal treatment of the pristine and contaminated Cd/Zn hyperaccumulators for bio-oil production and heavy metal separation. ACS Sustain. Chem. Eng. 10, 603–612. https://doi.org/10.1021/acssuschemeng.1c07151.

Danso-Boateng, E., Ross, A.B., Mariner, T., Hammerton, J., Fitzsimmons, M., 2022. Hydrochars produced by hydrothermal carbonisation of seaweed, coconut shell and oak: effect of processing temperature on physicochemical adsorbent characteristics. SN Appl. Sci. 4, 1–15. https://doi.org/10.1007/S42452-022-05085-X/TABLES/3.

Dastyar, W., Raheem, A., He, J., Zhao, M., 2019. Biofuel production using thermochemical conversion of heavy metal-contaminated biomass (HMCB) harvested from phytoextraction process. Chem. Eng. J. 358, 759–785. https://doi.org/10.1016/J.CEJ.2018.08.111.

Ding, D., Zhou, L., Kang, F., Yang, S., Chen, R., Cai, T., Duan, X., Wang, S., 2020. Synergistic adsorption and oxidation of ciprofloxacin by biochar derived from metal-enriched phytoremediation plants: experimental and computational insights. ACS Appl. Mater. Interfaces 12, 53788–53798. https://doi.org/10.1021/acsami.0c15861.

Eivazihollagh, A., Bäckström, J., Dahlström, C., Carlsson, F., Ibrahem, I., Lindman, B., Edlund, H., Norgren, M., 2017. One-pot synthesis of cellulose-templated copper nanoparticles with antibacterial properties. Mater. Lett. 187, 170–172. https://doi.org/10.1016/J.MATLET.2016.10.026.

Gao, Y., Wang, X., Wang, J., Li, X., Cheng, J., Yang, H., Chen, H., 2013. Effect of residence time on chemical and structural properties of hydrochar obtained by hydrothermal carbonization of water hyacinth. Energy 58, 376–383. https://doi.org/10.1016/J.ENERGY.2013.06.023.

Golia, E.E., 2023. The impact of heavy metal contamination on soil quality and plant nutrition. Sustainable management of moderate contaminated agricultural and urban soils, using low cost materials and promoting circular economy. Sustain Chem Pharm 33, 101046. https://doi.org/10.1016/J.SCP.2023.101046.

Gong, X., Huang, D., Liu, Y., Zeng, G., Wang, R., Wei, J., Huang, C., Xu, P., Wan, J., Zhang, C., 2018. Pyrolysis and reutilization of plant residues after phytoremediation

of heavy metals contaminated sediments: for heavy metals stabilization and dye adsorption. Bioresour. Technol. 253, 64–71. https://doi.org/10.1016/j.biortech.2018.01.018.
Guidi Nissim, W., Labrecque, M., 2023. Field assessment of trace element phytoextraction by different Populus clones established on brownfields in southern Quebec (Canada). Int. J. Phytoremediation 25, 283–292. https://doi.org/10.1080/15226514.2022.2074964.
Han, Z., Guo, Z., Zhang, Y., Xiao, X., Xu, Z., Sun, Y., 2018. Pyrolysis characteristics of biomass impregnated with cadmium, copper and lead: influence and distribution. Waste Biomass Valorization 9, 1223–1230. https://doi.org/10.1007/s12649-017-0036-5.
He, C., Giannis, A., Wang, J.Y., 2013. Conversion of sewage sludge to clean solid fuel using hydrothermal carbonization: hydrochar fuel characteristics and combustion behavior. Appl. Energy 111, 257–266. https://doi.org/10.1016/J.APENERGY.2013.04.084.
He, J., Strezov, V., Kumar, R., Weldekidan, H., Jahan, S., Dastjerdi, B.H., Zhou, X., Kan, T., 2019. Pyrolysis of heavy metal contaminated Avicennia marina biomass from phytoremediation: characterisation of biomass and pyrolysis products. J. Clean. Prod. 234, 1235–1245. https://doi.org/10.1016/J.JCLEPRO.2019.06.285.
İnci, D., Aydın, R., 2017. Potentiometric studies on complexation of Cu(II) ion with methyl/nitro-substituted 1,10-phenanthrolines and selected amino acids. J. Solut. Chem. 46, 124–138. https://doi.org/10.1007/S10953-016-0551-1/FIGURES/7.
Isichei, TinaO., Okieimen, FelixE., 2014. Adsorption of 2-nitrophenol onto water hyacinth activated carbon-kinetics and equilibrium studies. Environ. Pollut. 3, p99. https://doi.org/10.5539/EP.V3N4P99.
Islam, M.T., Sultana, A.I., Chambers, C., Saha, S., Saha, N., Kirtania, K., Reza, M.T., 2022. Recent progress on emerging applications of hydrochar. Energies 15, 9340. https://doi.org/10.3390/EN15249340. 2022, Vol. 15, Page 9340.
Jain, A., Balasubramanian, R., Srinivasan, M.P., 2016. Hydrothermal conversion of biomass waste to activated carbon with high porosity: a review. Chem. Eng. J. 283, 789–805. https://doi.org/10.1016/J.CEJ.2015.08.014.
Jiang, L., Li, K., Xia, L., Gao, J., Tang, L., Jia, Y., 2023. KOH-modified hydrochar produced from Cd/Zn hyperaccumulator Sedum Alfredii Hance for aqueous Cd(II) removal: behavior and mechanism. J. Environ. Chem. Eng. 11, 110925. https://doi.org/10.1016/J.JECE.2023.110925.
Kafle, A., Timilsina, A., Gautam, A., Adhikari, K., Bhattarai, A., Aryal, N., 2022. Phytoremediation: mechanisms, plant selection and enhancement by natural and synthetic agents. Environmental Advances 8, 100203. https://doi.org/10.1016/J.ENVADV.2022.100203.
Kang, S., Li, X., Fan, J., Chang, J., 2012. Characterization of hydrochars produced by hydrothermal carbonization of lignin, cellulose, d-xylose, and wood meal. Ind. Eng. Chem. Res. 51, 9023–9031. https://doi.org/10.1021/IE300565D/ASSET/IMAGES/LARGE/IE-2012-00565D_0011.JPEG.
Khalifa, E., Rzig, B., Chakroun, R., Nouagui, H., Hamrouni, B., 2019. Application of response surface methodology for chromium removal by adsorption on low-cost biosorbent. Chemometr. Intell. Lab. Syst. 189, 18–26. https://doi.org/10.1016/j.chemolab.2019.03.014.
Kim, D., Lee, K., Park, K.Y., 2014. Hydrothermal carbonization of anaerobically digested sludge for solid fuel production and energy recovery. Fuel 130, 120–125. https://doi.org/10.1016/J.FUEL.2014.04.030.
Kimbi Yaah, V.B., Zbair, M., Botelho de Oliveira, S., Ojala, S., 2021. Hydrochar-derived adsorbent for the removal of diclofenac from aqueous solution. Nanotechnology for Environmental Engineering 6, 1–12. https://doi.org/10.1007/S41204-020-00099-5/FIGURES/9.
Kozyatnyk, I., Benavente, V., Weidemann, E., Gentili, F.G., Jansson, S., 2023. Influence of hydrothermal carbonization conditions on the porosity, functionality, and sorption properties of microalgae hydrochars. Sci. Rep. 13, 1–10. https://doi.org/10.1038/s41598-023-35331-0. 2023 13:1.
Kumar Mishra, R., 2022. Pyrolysis of low-value waste switchgrass: physicochemical characterization, kinetic investigation, and online characterization of hot pyrolysis vapours. Bioresour. Technol. 347, 126720. https://doi.org/10.1016/J.BIORTECH.2022.126720.
Kupeta, A.J.K., Naidoo, E.B., Ofomaja, A.E., 2018. Kinetics and equilibrium study of 2-nitrophenol adsorption onto polyurethane cross-linked pine cone biomass. J. Clean. Prod. 179, 191–209. https://doi.org/10.1016/J.JCLEPRO.2018.01.034.
Li, Z., Liu, Y., Liang, Y., Wang, H., Yang, F., 2023. Study of the optimization and kinetics of the surfactant-induced ultrasonic-assisted extraction of perilla seed oil: free radical scavenging capacity and physicochemical and functional characteristics. Sustain Chem Pharm 32, 100977. https://doi.org/10.1016/J.SCP.2023.100977.
Li, Z., Sellaoui, L., Luiz Dotto, G., Bonilla-Petriciolet, A., Ben Lamine, A., 2019. Understanding the adsorption mechanism of phenol and 2-nitrophenol on a biopolymer-based biochar in single and binary systems via advanced modeling analysis. Chem. Eng. J. 371, 1–6. https://doi.org/10.1016/J.CEJ.2019.04.035.
Liaqat, M., Iqbal, T., Maryam, I., Riaz, K.N., Afsheen, S., Sohaib, M., Al-Zaqri, N., Warad, I., Al-Fatesh, A.S., 2024. Enhancing photocatalytic activity: investigating the synthesis and characterization of BiVO4/Cu2O/graphene ternary nanocomposites. J. Photochem. Photobiol. Chem. 446, 115122. https://doi.org/10.1016/J.JPHOTOCHEM.2023.115122.
Lin, H., Li, Q., Zhang, L., Zhang, S., Hu, X., 2022. Hydrothermal carbonization of sawdust with the bio-oil of same origin impacts evolution of structures of hydrochar. Fuel Process. Technol. 238, 107516. https://doi.org/10.1016/J.FUPROC.2022.107516.
Liu, D., Zhao, X., Su, R., Hao, Z., Jia, B., Li, S., Dong, L., 2019. Highly porous graphitic activated carbons from lignite via microwave pretreatment and iron-catalyzed graphitization at low-temperature for supercapacitor electrode materials. Processes 7, 300. https://doi.org/10.3390/PR7050300. 2019, Vol. 7, Page 300.
Liu, J., Zhao, C., Zhang, Z., Liao, J., Liu, Y., Cao, X., Yang, J., Yang, Y., Liu, N., 2016. Fluorine effects on U(VI) sorption by hydroxyapatite. Chem. Eng. J. 288, 505–515. https://doi.org/10.1016/J.CEJ.2015.12.045.
Liu, T., Chen, Zhenshan, Li, Z., Fu, H., Chen, G., Feng, T., Chen, Zhang, 2021. Preparation of magnetic hydrochar derived from iron-rich Phytolacca acinosa Roxb. for Cd removal. Sci. Total Environ. 769, 145159. https://doi.org/10.1016/J.SCITOTENV.2021.145159.
Luo, Y., Guo, W., Ngo, H.H., Nghiem, L.D., Hai, F.I., Zhang, J., Liang, S., Wang, X.C., 2014. A review on the occurrence of micropollutants in the aquatic environment and their fate and removal during wastewater treatment. Sci. Total Environ. 473, 619–641. https://doi.org/10.1016/J.SCITOTENV.2013.12.065. –474.
Ma, Hongfang, Xu, Z., Wang, W., Gao, X., Ma, Huifang, 2019. Adsorption and regeneration of leaf-based biochar for p -nitrophenol adsorption from aqueous solution. RSC Adv. 9, 39282–39293. https://doi.org/10.1039/C9RA07943B.
Makhado, E., Motshabi, B.R., Allouss, D., Ramohlola, K.E., Modibane, K.D., Hato, M.J., Jugade, R.M., Shaik, F., Pandey, S., 2022. Development of a ghatti gum/poly (acrylic acid)/TiO2 hydrogel nanocomposite for malachite green adsorption from aqueous media: statistical optimization using response surface methodology. Chemosphere 306, 135524. https://doi.org/10.1016/J.CHEMOSPHERE.2022.135524.
Moretti, A., Sharova, V., Carvalho, D.V., Boulineau, A., Porcher, W., de Meatza, I., Passerini, S., 2019. A comparison of formation methods for graphite//LiFePO4 cells. Batter Supercaps 2, 240–247. https://doi.org/10.1002/BATT.201800109.
Mosa, A., El-Ghamry, A., Tolba, M., 2018. Functionalized biochar derived from heavy metal rich feedstock: phosphate recovery and reusing the exhausted biochar as an enriched soil amendment. Chemosphere 198, 351–363. https://doi.org/10.1016/J.CHEMOSPHERE.2018.01.113.
Navarro, A.E., Cuizano, N.A., Lazo, J.C., Sun-Kou, M.R., Llanos, B.P., 2009. Comparative study of the removal of phenolic compounds by biological and non-biological adsorbents. J. Hazard Mater. 164, 1439–1446. https://doi.org/10.1016/J.JHAZMAT.2008.09.077.
Orozco, C.I., Freire, M.S., Gómez-Díaz, D., González-Álvarez, J., 2023. Removal of copper from aqueous solutions by biosorption onto pine sawdust. Sustain Chem Pharm 32, 101016. https://doi.org/10.1016/J.SCP.2023.101016.
Pauletto, P.S., Moreno-Pérez, J., Hernández-Hernández, L.E., Bonilla-Petriciolet, A., Dotto, G.L., Salau, N.P.G., 2021. Novel biochar and hydrochar for the adsorption of 2-nitrophenol from aqueous solutions: an approach using the PVSDM model. Chemosphere 269, 128748. https://doi.org/10.1016/J.CHEMOSPHERE.2020.128748.
Petrović, J., Ercegović, M., Simić, M., Kalderis, D., Koprivica, M., Milojković, J., Radulović, D., 2023. Novel Mg-doped pyro-hydrochars as methylene blue adsorbents: adsorption behavior and mechanism. J. Mol. Liq. 376, 121424. https://doi.org/10.1016/j.molliq.2023.121424.
Raheem, A., He, Q., Mangi, H., Areeprasert, C., Ding, L., Yu, G., 2022. Roles of Heavy Metals during Pyrolysis and Gasification of Metal-Contaminated Waste Biomass: A Review. https://doi.org/10.1021/acs.energyfuels.1c04051.
Sachan, D., Das, G., 2024. Selective adsorption of drug micropollutants from synthetic wastewater using hydrochar derived from carbonisation of unused leaves. Int. J. Environ. Anal. Chem. https://doi.org/10.1080/03067319.2021.2015583.
Sevilla, M., Fuertes, A.B., 2009. The production of carbon materials by hydrothermal carbonization of cellulose. Carbon N Y 47, 2281–2289. https://doi.org/10.1016/J.CARBON.2009.04.026.
Tu, W., Liu, Y., Xie, Z., Chen, M., Ma, L., Du, G., Zhu, M., 2021. A novel activation-hydrochar via hydrothermal carbonization and KOH activation of sewage sludge and coconut shell for biomass wastes: preparation, characterization and adsorption properties. J. Colloid Interface Sci. 593, 390–407. https://doi.org/10.1016/J.JCIS.2021.02.133.

Vakili, M., Mojiri, A., Kindaichi, T., Cagnetta, G., Yuan, J., Wang, B., Giwa, A.S., 2019. Cross-linked chitosan/zeolite as a fixed-bed column for organic micropollutants removal from aqueous solution, optimization with RSM and artificial neural network. J. Environ. Manag. 250, 109434. https://doi.org/10.1016/j.jenvman.2019.109434.

Wang, Y., Lü, J., Feng, D., Guo, S., Li, J., 2020. A biosorption-pyrolysis process for removal of Pb from aqueous solution and subsequent immobilization of Pb in the char. Water 12, 2381. https://doi.org/10.3390/W12092381. 2020, Vol. 12, Page 2381.

Wei, X., Wang, X., Gao, B., Zou, W., Dong, L., 2020. Facile ball-milling synthesis of CuO/biochar nanocomposites for efficient removal of reactive red 120. ACS Omega 5, 5748–5755. https://doi.org/10.1021/ACSOMEGA.9B03787/ASSET/IMAGES/LARGE/AO9B03787_0005.JPEG.

Wei, Z., Gu, H., Van Le, Q., Peng, W., Lam, S.S., Yang, Y., Li, C., Sonne, C., 2021. Perspectives on phytoremediation of zinc pollution in air, water and soil. Sustain Chem Pharm 24, 100550. https://doi.org/10.1016/J.SCP.2021.100550.

Xu, Z.X., Song, H., Li, P.J., He, Z.X., Wang, Q., Wang, K., Duan, P.G., 2020. Hydrothermal carbonization of sewage sludge: effect of aqueous phase recycling. Chem. Eng. J. 387, 123410. https://doi.org/10.1016/J.CEJ.2019.123410.

Yang, J., 2010. Heavy metal removal and crude bio-oil upgrading from Sedum plumbizincicola harvest using hydrothermal upgrading process. Bioresour. Technol. 101, 7653–7657. https://doi.org/10.1016/J.BIORTECH.2010.04.095.

Zeng, Z., Zhang, S. Da, Li, T.Q., Zhao, F.L., He, Z.L., Zhao, H.P., Yang, X.E., Wang, H.L., Zhao, J., Rafiq, M.T., 2013. Sorption of ammonium and phosphate from aqueous solution by biochar derived from phytoremediation plants. J. Zhejiang Univ. - Sci. B 14, 1152–1161. https://doi.org/10.1631/jzus.B1300102.

Zhang, J., Wang, Y., Wang, X., Wu, W., Cui, X., Cheng, Z., Yan, B., Yang, X., He, Z., Chen, G., 2022a. Hydrothermal conversion of Cd/Zn hyperaccumulator (Sedum alfredii) for heavy metal separation and hydrochar production. J. Hazard Mater. 423, 127122. https://doi.org/10.1016/J.JHAZMAT.2021.127122.

Zhang, L., Wang, Q., Wang, B., Yang, G., Lucia, L.A., Chen, J., 2015. Hydrothermal carbonization of corncob residues for hydrochar production. Energy Fuel. 29, 872–876. https://doi.org/10.1021/EF502462P/ASSET/IMAGES/LARGE/EF-2014-02462P_0005.JPEG.

Zhang, X., Liu, S., Wang, M., Ma, X., Sun, X., Liu, X., Wang, L., Wang, W., 2022b. Hydrochar magnetic adsorbent derived from Chinese medicine industry waste via one-step hydrothermal route: mechanism analyses of magnetism and adsorption. Fuel 326, 125110. https://doi.org/10.1016/J.FUEL.2022.125110.

Zhang, Y., Chen, Z., Xu, W., Liao, Q., Zhang, H., Hao, S., Chen, S., 2020. Pyrolysis of various phytoremediation residues for biochars: chemical forms and environmental risk of Cd in biochar. Bioresour. Technol. 299, 122581. https://doi.org/10.1016/j.biortech.2019.122581.

Zhang, Y.C., Tang, J.Y., Wang, G.L., Zhang, M., Hu, X.Y., 2006. Facile synthesis of submicron Cu2O and CuO crystallites from a solid metallorganic molecular precursor. J. Cryst. Growth 294, 278–282. https://doi.org/10.1016/J.JCRYSGRO.2006.06.038.

Zhou, L., Zhu, X., Chi, T., Liu, B., Du, C., Yu, G., Wu, H., Chen, H., 2022a. Reutilization of manganese enriched biochar derived from Phytolacca acinosa Roxb. residue after phytoremediation for lead and tetracycline removal. Bioresour. Technol. 345, 126546. https://doi.org/10.1016/J.BIORTECH.2021.126546.

Zhou, S., Huo, X., Hua, M., Luo, G., Fan, J., Clark, J.H., Zhang, S., 2022b. Insights on the effect of heavy metals on subcritical hydrothermal recycling of heavy metal-contaminated biomass and its derived porous carbon properties using Cu as a case. ACS ES and T Engineering 2, 2245–2253. https://doi.org/10.1021/ACSESTENGG.2C00207/ASSET/IMAGES/LARGE/EE2C00207_0006.JPEG.